JGR Earth Surface

RESEARCH ARTICLE
10.1029/2024JF007867

A New Approach to Account for Species-Specific Sand Capture by Plants in an Aeolian Sediment Transport and Coastal Dune Building Model

Quentin Laporte-Fauret[1], Meagan Wengrove[1], Peter Ruggiero[2], Sally D. Hacker[3], Nicholas Cohn[4], Phoebe L. Zarnetske[5], and Candice D. Piercy[6]

[1]Civil and Construction Engineering, Oregon State University, Corvallis, OR, USA, [2]College of Earth, Ocean, and Atmospheric Sciences, Oregon State University, Corvallis, OR, USA, [3]Department of Integrative Biology, Oregon State University, Corvallis, OR, USA, [4]U.S. Army Engineer Research and Development Center, Coastal and Hydraulics Laboratory—Field Research Facility, Duck, NC, USA, [5]Department of Integrative Biology, Michigan State University, East Lansing, MI, USA, [6]U.S. Army Engineer Research and Development Center, Environmental Laboratory, Vicksburg, MS, USA

Key Points:

- A new modeling approach incorporates species-specific dune grass characteristics on sand capture efficiency and dune bedform shape
- The species-specific morphology metrics of the three grasses produce sand capture efficiencies similar to a wind tunnel experiment
- The new model simulates species-specific dune bedforms, consistent with dune field observations associated with the three plant species

Supporting Information:

Supporting Information may be found in the online version of this article.

Correspondence to:

Q. Laporte-Fauret,
quentin.laporte-fauret@oregonstate.edu

Citation:

Laporte-Fauret, Q., Wengrove, M., Ruggiero, P., Hacker, S. D., Cohn, N., Zarnetske, P. L., & Piercy, C. D. (2024). A new approach to account for species-specific sand capture by plants in an aeolian sediment transport and coastal dune building model. *Journal of Geophysical Research: Earth Surface*, *129*, e2024JF007867. https://doi.org/10.1029/2024JF007867

Received 6 JUN 2024
Accepted 19 NOV 2024

Author Contributions:

Conceptualization: Quentin Laporte-Fauret, Meagan Wengrove, Peter Ruggiero, Sally D. Hacker, Nicholas Cohn, Candice D. Piercy
Formal analysis: Quentin Laporte-Fauret
Funding acquisition: Meagan Wengrove, Peter Ruggiero, Sally D. Hacker
Investigation: Quentin Laporte-Fauret
Methodology: Quentin Laporte-Fauret
Project administration: Meagan Wengrove, Peter Ruggiero, Sally D. Hacker
Software: Quentin Laporte-Fauret, Nicholas Cohn
Supervision: Meagan Wengrove, Peter Ruggiero, Sally D. Hacker, Nicholas Cohn
Validation: Quentin Laporte-Fauret
Visualization: Quentin Laporte-Fauret

Abstract Vegetation plays a crucial role in coastal dune building. Species-specific plant characteristics can modulate sediment transport and dune shape, but this factor is absent in most dune building numerical models. Here, we develop a new approach to implement species-specific vegetation characteristics into a process-based aeolian sediment transport model. Using a three-step approach, we incorporated the morphological differences of three dune grass species dominant in the US Pacific Northwest coast (European beachgrass *Ammophila arenaria*, American beachgrass *A. breviligulata*, and American dune grass *Leymus mollis*) into the model AeoLiS. First, we projected the tiller frontal area of each grass species onto a high resolution grid and then re-scaled the grid to account for the associated vegetation cover for each species. Next, we calibrated the bed shear stress in the numerical model to replicate the actual sand capture efficiency of each species, as measured in a previously published wind tunnel experiment. Simulations were then performed to model sand bedform development within the grass canopies with the same shoot densities for all species and with more realistic average field densities. The species-specific model shows a significant improvement over the standard model by (a) accurately simulating the sand capture efficiency from the wind tunnel experiment for the grass species and (b) simulating bedform morphology representative of each species' characteristic bedform morphology using realistic field vegetation density. This novel approach to dune modeling will improve spatial and temporal predictions of dune morphologic development and coastal vulnerability under local vegetation conditions and variations in sand delivery.

Plain Language Summary Coastal dunes form through complex interactions between wind, waves, and vegetation, where plants trap sand and promote dune growth. Species-specific plant characteristics can modulate sediment transport and dune shape, but this factor is rarely incorporated into dune growth models. In this study, we developed a new approach to make dune-building models more realistic by including the unique features of three common dune grass species found along the U.S. Pacific Northwest coast (European beachgrass *Ammophila arenaria*, American beachgrass *A. breviligulata*, and American dune grass *Leymus mollis*). First, we calculated the frontal areas of each of the three plant species and projected that area onto a horizontal grid. We then integrated these grids into a standard aeolian sediment transport model and calibrated the effect of vegetation on shear velocity using a previous wind tunnel experiment. The results show that our species-specific model provides a better picture of how each species of grass shape dunes compared to the standard model without these species-specific considerations. This improvement could help scientists make better predictions about how coastal dunes will form and change over time, which is especially important as coastlines face more extreme weather and rising sea levels.

1. Introduction

Coastal dunes are common landforms that may develop on sandy shorelines, which cover roughly a third of the world's coastlines (Luijendijk et al., 2018). These shore-parallel aeolian landforms develop mainly on wave-dominated temperate coasts with moderate to high sediment supply through complex interactions involving marine, aeolian, and vegetative processes (Biel et al., 2019; Cohn et al., 2018; Hacker et al., 2012; Hesp, 2002;

Writing – original draft: Quentin Laporte-Fauret
Writing – review & editing: Meagan Wengrove, Peter Ruggiero, Sally D. Hacker, Nicholas Cohn, Phoebe L. Zarnetske, Candice D. Piercy

Maun, 1998; Maun & Perumal, 1999; Nordstrom, 2000). The presence of vegetation promotes windblown sand deposition, which in turn can stimulate vegetation growth. Eventually, this positive feedback between sand deposition and plant growth builds and stabilizes coastal dunes (Charbonneau et al., 2021; Emery & Rudgers, 2014; Maun, 1998; Zarnetske et al., 2012, 2013). Coastal dunes evolve over a range of temporal and spatial scales, resulting in wide variability in dune shape and size (Biel et al., 2019; Hacker et al., 2012; Jay et al., 2022; Keijsers et al., 2015; Sherman & Bauer, 1993; Stive et al., 2002; Walker et al., 2017; Zarnetske et al., 2015).

Vegetated coastal dunes provide a range of ecosystem services such as flood protection, species diversity conservation, and carbon sequestration (Barbier et al., 2011; Barbour et al., 1985; Charbonneau et al., 2016; Martinez et al., 2013; Provoost et al., 2011; Pye et al., 2014; Stepanek, 2023). However, dunes are under threat from increasing anthropogenic pressures (Merkens et al., 2018; Neumann et al., 2015), including sea-level rise, leading to increased exposure to flooding and erosion (Alfieri et al., 2015; Cooper et al., 2020; Lionello et al., 2006; Rojas et al., 2012; Seabloom et al., 2013; Vousdoukas et al., 2016, 2020).

To better understand the development of coastal dunes and their complex ecomorphodynamic interactions with vegetation, techniques including statistical models (Biel et al., 2019; Jay et al., 2022; Keijsers et al., 2016), process based models (Durán & Moore, 2013; Hoonhout & de Vries, 2016; Luna et al., 2011), and coupled aeolian and marine models (Cohn et al., 2019; Hovenga et al., 2022; Roelvink & Costas, 2019) have been developed. De Groot et al. (2011) created the Dune-Beach Vegetation (DUBEVEG) model, based on cellular automata, to simulate dune formation (from the DECAL Algorithm (Baas, 2002)) and vegetation dynamics (from the NUCOM model (van Oene et al., 1999)). The model has been applied to a variety of topics, including long-term dune evolution with sea-level rise and vegetation growth (Keijsers et al., 2016), beach width change impacts on the development of coastal dune systems (Galiforni-Silva et al., 2019), and groundwater levels and sediment supply for aeolian dune development (Galiforni-Silva et al., 2018). The Coastal Dune Model (CDM), developed from the work of Sauermann et al. (2001) and Durán and Herrmann (2006), simulates the evolution of coastal vegetated dunes (Durán & Moore, 2013). This model resolves airflow, sediment transport, and vegetation growth with several differential equations characterizing their interactions and feedbacks, and has been used to improve understanding of the formation of linear dunes, parabolic dunes, and barchan dunes (Durán & Herrmann, 2006; Parteli et al., 2009; Schwämmle & Herrmann, 2005). The CDM was also used to assess the processes controlling coastal foredune development (Goldstein et al., 2017; Moore et al., 2016) and post-storm dune recovery (Durán & Moore, 2015). Recently, a process-based aeolian sediment transport model, AeoLiS, was developed to simulate supply limited sediment transport situations on coastal dune building (de Vries et al., 2023; Hoonhout & de Vries, 2016). To model variability in coastal dune landforms, processes have been implemented in AeoLiS that include interaction between the wind field and dune morphology (Kroy et al., 2002; Sauermann et al., 2001; Weng et al., 1991), sand deposition in vegetation (Dickey et al., 2023), and sand moisture and swash zone effects (Hallin et al., 2023).

In many numerical models, the effect of vegetation on shear velocity (u^*) is effectively partitioned into a shear component that acts on the bare surface/sand (e.g., particle shear as u_s^*) and a drag component that acts on the roughness elements (e.g., vegetation as u_{veg}^*) (Raupach, 1992; Raupach et al., 1993; Shao, 2008; Webb et al., 2014). Within aeolian transport models the influence of vegetation on imposed shear is highly simplified by implementing what is called a "shear coupler" into the model, which effectively modifies the shear velocity for the presence of the roughness element, such as vegetation.

The Raupach (1992) formulation uses a dimensionless roughness factor to describe the ability of vegetation to reduce flow and trap wind-blown sand. The roughness factor for coastal grasses, as implemented in Raupach (1992), is derived from drag and geometry data from desert shrubs, which is assumed to be similar to that of coastal grasses (Durán & Herrmann, 2006). The model idealizes a triangular shaped area downwind of the vegetation where there is no shear stress imposed on the surface due to blockage of the vegetation leading to no sediment mobilization in that region. Various two-dimensional ecomorphodynamic models, including CDM and Aeolis, include a presentation of the Raupach (1992) formulation to represent vegetation effects on bed shear stress. In these tools, the triangular area of no shear stress and the unaffected area are weighed over one model grid cell. The model implementation assumes that all shear stress reduction occurs in a single grid cell, making it suitable for cases with relatively larger grid cells (e.g., roughly 1 m) as opposed to small grid cells (e.g., 0.01 m scale). Limitations of the Raupach (1992) model include that it does not consider irregular roughness elements or irregular roughness element distribution over a surface. Instead, this approach assumes that a large roughness

element can reduce bed shear stress to the same degree as several small roughness elements. Additionally, Raupach (1992) assumes that there is no sheltering occurring downwind of the roughness elements. These limitations make Raupach (1992) more suitable for wind drag imposed on solid elements rather than for porous elements such as vegetation (Okin, 2008).

More recently, Okin (2008) developed an alternative shear coupling approach in which shear stress reduction is computed using a probability distribution of unvegetated to vegetated areas. The Okin (2008) approach (built on experimental observations of Bradley & Mulhearn, 1983) assumes that the shear stress downwind of a porous roughness element is not a fixed value but instead increases gradually downwind using an empirical relation that involves the shear stress, the leeward distance, and the vegetation height. The Okin (2008) model contains two coefficients that adjust for the influence of vegetation on both shear stress reduction, R_0, and on downwind shear stress recovery C_1 (see Equation 13).

The downwind flow through vegetation depends on many factors, such as the initial wind speed, the vegetation density, distribution, and morphology, and the plant porosity (Cheng et al., 2018; Gillies et al., 2014; Hesp, 1983; Youssef et al., 2012). For example, wind speed profile measurements in coastal vegetation show decreasing wind speed downwind of the plant canopy with increasing plant cover (Buckley, 1987; Hesp, 1983, 1989). This downwind distance is called the canopy drag length (L_C) and describes the distance required for the flow to adjust to the presence of vegetation (Belcher et al., 2003; Rominger & Nepf, 2011). Recent field and wind tunnel experiments conducted by Hesp et al. (2019) highlight that as vegetation density increases, drag increases, and thus flow deceleration increases. Even in sparse vegetation, where cover was as low as 12%, the wind speed dropped by 50% within 50 cm downwind of the leading plant (Hesp et al., 2019). Finally, for the same wind speed, Hesp et al. (2019) found that as the vegetation density decreased, the height of the developed bedform decreased and the bedform formed further downwind of the leading plant.

The distance between the leading plant and the location in which deposition begins has also been quantified in the field by Dickey et al. (2023), who made a series of measurements through sparsely vegetated monocultures of two common dune grass species (European beachgrass *Ammophila arenaria* and American dune grass *Leymus mollis*) in the US Pacific Northwest. They developed a new empirical model of sand deposition within sparsely vegetated dunes by determining the deposition lag length (L_D), which depends on both the vegetation cover and L_C. Through three cross-shore transects, Dickey et al. (2023) found that the deposition lag length increased with decreasing plant cover (i.e., L_D values of 7.9 m with 10% cover of *A. arenaria* and *L. mollis*, 1.9 m with 17.2% cover of *A. arenaria*, and 0.4 m with 20.6% cover of *A. arenaria*). This field derived relationship was incorporated into the Raupach (1992) and Okin (2008) shear coupler in AeoLiS (Dickey et al., 2023).

In addition to the recent studies of Hesp et al. (2019) and Dickey et al. (2023), there is mounting evidence that species-specific differences in plant morphology and growth form can lead to variable sand deposition and bedform morphology. For example, Charbonneau et al. (2021) conducted a wind tunnel experiment using three dune grass species on the US East coast and showed that the two native grasses to the US East coast (*Ammophila breviligulata* and *Panicum amarum*) built more elongated, high relief bedforms than the low-lying non-native grass (*Carex kobomugi*), which built lower and more symmetrical bedforms. Other field observations and wind tunnel experiments have shown similar patterns with the plant species that dominate the US Pacific Northwest coast (Biel et al., 2019; Hacker et al., 2012, 2019; Zarnetske et al., 2012, 2015). In that system, two non-native beachgrass species were introduced in the early twentieth century to stabilize the shifting sand environment (Wiedemann & Pickart, 1996). The non-native *Ammophila* species became invasive and spread widely creating foredunes that vary in size depending on sand supply and dune grass species composition and density (Biel et al., 2019; Hacker et al., 2012; Zarnetske et al., 2012). Under natural field conditions, due to its vertical growth form and relatively high shoot density, *A. arenaria* traps more sand for a given area and builds tall and narrow dunes. By comparison, *A. breviligulata* has a lateral growth form but lower shoot density, resulting in less vertical sand capture and dunes that are shorter and wider than those with *A. arenaria*. Finally, the native grass *L. mollis* has a lateral growth form and the lowest shoot density, resulting in even shorter and wider dunes. However, in a wind tunnel experiment in which tiller density was controlled, Zarnetske et al. (2012) found that sand capture efficiency on a per tiller basis was greatest for the native *L. mollis*, intermediate for *A. breviligulata*, and lowest for *A. arenaria*, which reflected the weight of the shoots from stout for the native grass to thin for the European grass. Thus, this experiment showed that the combination of tiller size and tiller density are the main variables influencing sand capture efficiency and thus dune morphology.

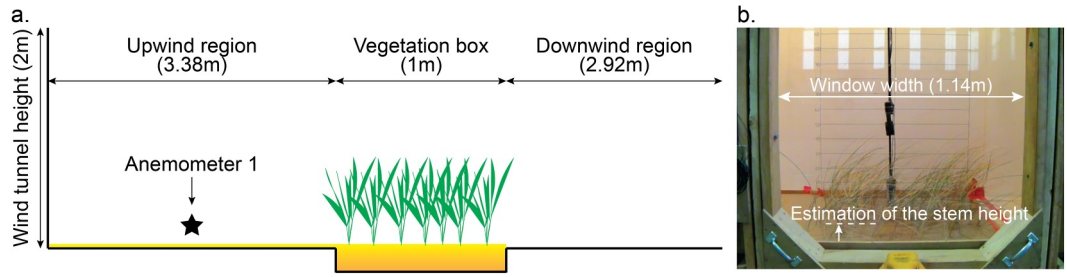

Figure 1. (a) Representation of the wind tunnel used in the experiment of Zarnetske et al. (2012), (b) Excerpt from video of a run with 152 tiller/m^2 of *Ammophila arenaria* under low (i.e., 6 m/s) wind speed. For the study, three tiller and stem heights were measured from the videos for an average ± SD tiller height (m) of 0.39 ± 0.05 and stem height (m) of 0.08 ± 0.005.

Currently, there is a need to improve vegetation parameterizations in coastal dune morphological change models. Although field and experimental studies have demonstrated that different dune grass species lead to varying dune morphologies due to differences in growth form, shoot density, shoot morphology, and sand capture efficiency, most existing numerical models apply a generalized approach to vegetation. This simplification fails to capture the distinct effects of species-specific traits on dune development. Addressing this gap, by refining vegetation parameterizations, is essential for more accurate ecomorphodynamic modeling. The objective of the present study is to build on and enhance the process-based aeolian transport and dune morphologic change model AeoLiS (de Vries et al., 2023; Hoonhout & de Vries, 2016) by incorporating species-specific characteristics of three dominant dune grass species (European beachgrass *Ammophila arenaria*, American beachgrass *A. breviligulata*, and American dune grass *Leymus mollis*) on the US Pacific Northwest coast into the Okin (2008) shear coupler. We used the previously described wind tunnel experiment of Zarnetske et al. (2012) that measured the sand capture efficiency of the three dune grass species predominantly found in the Pacific Northwest of the US, but also in other places around the world, to calibrate the coefficient related to shear stress reduction (i.e., R_0) in the Okin (2008) shear stress partitioning model for each species. Finally, we used the updated model to account for reduced sand capture through sparse vegetation (Dickey et al., 2023) to simulate sand trapping and bedform development in the presence of the three species of vegetation for a constant density among species and for the average densities of each species found in the field.

2. Methods

2.1. Wind Tunnel Experiment

To calibrate AeoLiS, we used sand capture efficiency (*Ce*) data measured from a wind tunnel experiment using three species of dune grasses (i.e., *Ammophila arenaria*, *A. breviligulata*, and *Leymus mollis*) dominant on the US Pacific Northwest coast (see Zarnetske et al. (2012) for detailed methods and illustrations of the experiment). The grasses were planted in 1-m^2 boxes at three target densities of 125, 250, and 500 tillers/m^2 with three replicates per species by tiller density combination (i.e., 27 boxes, Table S1 in Supporting Information S1) and exposed to blowing sand at two wind speeds of 6 m/s and 9.5 m/s (Figure 1).

Sand capture efficiency, *Ce*, from the wind tunnel experiment was measured as the proportion of the sand captured in the vegetated boxes and was computed as:

$$Ce = \frac{b_f - b_i}{s_{in}} \quad (1)$$

Where b_i and b_f are the initial and final sand box mass (kg), respectively and s_{in} (kg) is the sand provided upwind to the vegetation, computed as the difference between the initial and final upstream sand mass. The volumetric sediment transport rate (q) per unit tunnel width was computed as:

$$q = \frac{s_{in}}{\rho_s \, t \, w} \quad (2)$$

where ρ_s is the sand density (1,600 kg/m^3), t is the experimental run time (1,200 s or 4,800 s) and w is the tunnel width (1 m).

To compare the results between the species and densities within a wind speed, the sand capture efficiency (i.e., Ce) of each experimental run was normalized as:

$$Ce_{norm} = \frac{Ce}{q^*} \tag{3}$$

where q^* is the non-dimensional volumetric sediment transport rate, computed as:

$$q^* = \frac{q}{d\sqrt{\frac{\rho_s - \rho_a}{\rho_a} g\, d}} \tag{4}$$

where ρ_a is the air density (1.2 kg/m^3), d is the median grain size (2.4×10^{-4} m), and g is the acceleration due to gravity (9.81 m/s). Finally, Zarnetske et al. (2012) applied a natural-log transformation to conform to the assumption of linear regression, transforming Ce_{norm} into $\ln(Ce_{\text{norm}})$.

2.2. Model Description

2.2.1. Sediment Transport

AeoLiS (de Vries et al., 2023; Hoonhout & de Vries, 2016) was developed to simulate aeolian transport and sediment availability for supply limited systems such as coastal environments. The model employs a multi-fraction aeolian sediment transport approach through an advection scheme with grain-size selectivity. The net entrainment (erosion minus deposition), computed for a range of grain size fractions, is determined by the difference between the saturated and actual sediment concentrations transported in the simulated air. Transport can be restricted by sediment availability in the surface bed layer due to the presence of non-erodible layers, grain armoring, or local moisture effects that are represented through modification of the threshold shear velocity for initiation of sediment transport.

In the model, a modified version of the Bagnold equation (Bagnold, 1937) is used to compute the equilibrium transport rate as follows:

$$Q = C\sqrt{\frac{d}{D}}\,\frac{\rho_a}{g}\,(u_* - u_{*,t})^3 \tag{5}$$

where Q is the aeolian sediment transport rate in the case of saturated transport (kg/m/s), D is the reference grain diameter (0.25 mm, Bagnold, 1937), C is a constant equal to 1.8 to represent the naturally graded sand generally found on dunes (Bagnold, 1941). The threshold shear velocity, $u_{*,t}$ (m/s) represents the shear velocity at which the surface grain movement is initiated and is computed using the formula of Bagnold (1937):

$$u_{*,t} = A\sqrt{\frac{\rho_s - \rho_a}{\rho_a} g\, d} \tag{6}$$

with A the non-dimensional empirical constant equal to 0.085. The shear velocity, u_* (m/s), is computed by using the logarithmic law of the wall:

$$u_* = u_z\,\frac{\kappa}{ln\left(\frac{z}{z_0}\right)} \tag{7}$$

where κ is the von Karman coefficient (0.4), z is the elevation (m), u_z is the wind speed (m/s) at the elevation z, and z_0 is the aerodynamic roughness length (m). The computation of z_0 is based on the recent formulation

developed by Van Rijn and Strypsteen (2020) and Strypsteen et al. (2021), which ensures a smooth transition from the non-transport regime to the transport regime, as:

$$z_0 = \frac{d_{90} + \alpha_1 \gamma_r d_{50} T_p^{\alpha_2}}{30} \tag{8}$$

with d_{90} approximated by $2d_{50}$ (m) where d_{50} is the median grain size, α_1 and α_2 are empirical coefficients equal to 15 and 1, respectively, γ_r is the ripple enhancement coefficient, which is equal to $1 + 1/T_p$, and T_p is the transport parameter computed as:

$$T_p = \frac{(u_{*,grain,stat})^2 - (u_{*,t})^2}{(u_{*,t})^2} \tag{9}$$

where $u_{*,grain,stat}$ is the shear velocity related to static grains (m/s) and is calculated by:

$$u_{*,grain,stat} = u_z \frac{\kappa}{ln\left(\frac{30 \cdot z}{d_{90}}\right)} \tag{10}$$

Finally, from Equation 5, the equilibrium transport rate is used through a 1D advection scheme (de Vries et al., 2014) as

$$\frac{\partial c}{\partial t} + u_z \frac{\partial c}{\partial x} = \frac{c_{sat} - c}{T} \tag{11}$$

with c the sediment mass per unit area (kg/m^2) through time t (s) and space x (m). The difference between the saturated sediment concentration c_{sat} (kg/m^2) and c divided by the adaptation time scale T (set to 0.1 s) allows for the characterization of the bed exchange (i.e., erosion and deposition patterns). Sand flux, Q, is related to concentration, c, by multiplying concentration by sand transport speed.

2.2.2. Vegetation

Vegetation was initially implemented in AeoLiS via a roughness element that has a percent cover and a height. The cover value in each grid cell, ρ_{veg}, ranges from 0 (no vegetation) to 1 (fully vegetated). Vegetation height was approximated according to $h_c = h_{c,max}\sqrt{\rho_{veg}}$ with h_c the height of the canopy (m), $h_{c,max}$ the maximum height of vegetation (m) and ρ_{veg} the vegetation cover fraction. The effect of vegetation on sediment transport can be quantified using either of the two shear stress partitioning models described, both of which are implemented in the standard AeoLiS model as follows. First, the formulation developed by Raupach (1992) and Raupach et al. (1993) is given as

$$\frac{u_{*,veg}}{u_*} = \frac{1}{\sqrt{1 + \Gamma \rho_{veg}}} \tag{12}$$

where Γ is a roughness parameter set to 16 for dune grass (Durán & Herrmann, 2006). The shear stress partitioning model developed by Okin (2008) was implemented in AeoLiS by the formulation:

$$\frac{u_{*,veg}}{u_*}(x) = R_0 + (1 - R_0)\left(1 + e^{-C_1 \frac{x}{h}}\right) \tag{13}$$

where $R_0 = u_{*,veg}/u_*$ for $x = 0$, x is the coordinate relative to the roughness element, C_1 is a factor controlling the shear stress recovery and h is the height of the roughness elements (m), where in AeoLiS, h is implemented as the height of the canopy (h_c). Based on the data of Bradley and Mulhearn (1983) using values of sand flow through fences, the best-fit values for the Okin formulation are $R_0 = 0.32$ and $C_1 = 4.8$.

Both the Raupach (1992) and Okin (2008) shear couplers implement shear reduction at the leading edge of the canopy, which does not consider the deceleration of wind speed through vegetation. As mentioned previously, full shear stress reduction may not occur until some distance into the canopy, especially for sparse canopies. To consider the deceleration of wind speed through dune grasses in particular, the length scale over which the wind equilibrates to the presence of the canopy, L_C (Belcher et al., 2003), and the lag length from the canopy leading edge to the leading edge of sand deposition in the canopy, L_D, were introduced and first implemented into the AeoLiS model by Dickey et al. (2023) as:

$$L_D = 0.95L_c - 0.09 \tag{14}$$

$$L_c = \frac{2(1-\Phi)\,h_c}{C_D\lambda} \tag{15}$$

where Φ is the fraction of dune grass shoot volume (m^3), C_D is the drag coefficient of each tiller, and λ is the frontal area of grass tillers per unit of bed area (m^2/m^2). These last three parameters are calculated by

$$\Phi = \alpha\, N_{tiller}\, w_{tiller}\, t_{tiller} \left(\frac{h_{tiller,stretch}}{h_{tiller,relax}}\right) \tag{16}$$

$$C_D = 1 + 10Re^{-\frac{2}{3}} \tag{17}$$

$$\lambda = \alpha\, N_{tiller}\, w_{tiller}\, h_{tiller} \tag{18}$$

where α and N_{tiller} are the average number of blades per stem and the density of tillers in the canopy, respectively, h_{tiller}, w_{tiller} and t_{tiller} represent the height (m), which can be measured from bed to the top of the longest shoot, the width (m), and the thickness (m) of the tillers, respectively. In the equation of the drag coefficient at the tiller scale (Equation 17, Rominger & Nepf, 2011), the Reynolds number is computed by $Re = u_z\, w_{tiller}/\upsilon$ with υ the air viscosity (m^2/s).

In the initial version developed by Dickey et al. (2023), the shear stress partitioning model was applied downwind of the leading edge of the canopy, then a mask was applied from the leading edge to the L_D value to remove morphological changes, preventing erosion in this area and forming a significant deposition gradient once the distance had been exceeded (Figure S1, blue line in Supporting Information S1). Here we modified the implementation by replacing this mask with a shift where the shear stress partitioning model is applied into the patch downwind of the distance computed by L_D. This implementation allows sediment mobilization downwind of the leading edge and reduces the deposition gradient in the patch (Figure S1, orange line in Supporting Information S1).

2.2.3. New Approach for Representing Vegetation Cover Based on Plant Morphology in AeoLiS

In the standard AeoLiS (version 2.1.0 for the purposes of this study) model, vegetation is implemented as percent cover but without consideration of the vegetation under different wind speeds and densities. We used a new approach in which we estimated the frontal area of tillers taking into account species-specific tiller morphology, tiller density, and bending under different wind speeds (Figure 2). First, we estimated the frontal area of tillers from the heights and widths of the stems and blades of the three species without wind (Figure 2). Second, we estimated how the frontal area changed for each species under different wind speeds. We reasoned that as wind speed increases, blade bending increases and frontal area decreases. However, increasing the tiller frontal area and tiller density can act to support adjacent blades and reduce the impact of wind on bending. Therefore, it is necessary to measure the change in frontal area of each species as a function of wind speed and tiller density.

To measure the frontal area of the three grass species, we used videos recorded during the wind tunnel experimental runs of Zarnetske et al. (2012) to measure tiller morphology under different wind speeds and tiller densities and to compute a metric for the blade bending or flexibility (Figure 1b). First, for each species, we measured the tiller height, stem height, and blade height (i.e., tiller height minus stem height) under all wind speeds and tiller density treatments. Then, for each species, we computed the relative blade height F_{sp} as the percent difference between blade height with and without wind (i.e., blade height is 100% without wind) for a

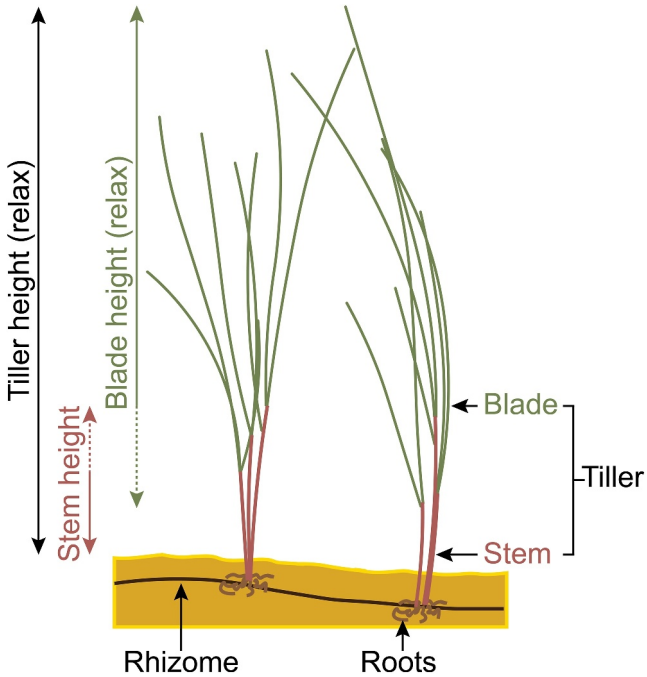

Figure 2. Schematic representation of the different parts of a dune grass tiller, including the stem, blades, roots, and rhizomes.

range of experimental tiller densities (Figure S2 in Supporting Information S1). We used these values to establish relationships of blade relative height (metric for blade bending or flexibility) of each species as a function of wind speed and tiller density:

$$F_{A.\ arenaria} = -4.12u + 1.95 \times 10^{-2} d_{veg} + 94.45 \quad (19)$$

$$F_{A.\ breviligulata} = -4.45u + 6.52 \times 10^{-3} d_{veg} + 98.32 \quad (20)$$

$$F_{L.\ mollis} = -4.60u + 3.62 \times 10^{-2} d_{veg} + 88.07 \quad (21)$$

where u is the wind speed (m/s) and d_{veg} is tiller density (tiller/m^2). These relationships had R^2 values of $R^2_{A.\ arenaria} = 0.97$, $R^2_{A.\ breviligulata} = 0.96$, and $R^2_{L.\ mollis} = 0.90$ (see Section 2.3 for R^2). The adjusted blade height, $h_{blade,sp,adjusted}$ (m), is then computed using the relaxed blade height of the species, $h_{blade,sp}$ (m), and the species-specific empirical equation for relative blade height, F_{sp}, by:

$$h_{blade,sp,adjusted} = h_{blade,sp} \times \left(\frac{F_{sp}}{100}\right) \quad (22)$$

Limits are applied with $h_{blade,sp,adjusted} = h_{blade,sp}$ if there is no wind and $h_{blade,sp,adjusted} = 0$ if F_{sp} is greater than 100, which indicates that the blade is bent over completely.

The tillers can now be represented as in Figure 3, with stem and multiple blades that have height that varies according to wind speed and density. Using the stem morphology (i.e., height and width) and the blade characteristics (i.e., adjusted height, width, and number of blades per stem) (metrics from Zarnetske et al., 2012; Laporte-Fauret et al., 2023, see Table S2 in Supporting Information S1), the frontal area of each tiller for each species, $\lambda_{tiller,sp}$ (m^2) can be computed by:

$$\lambda_{tiller,sp} = (w_{stem,sp} \times h_{stem,sp}) + ((w_{blade,sp} \times h_{blade,sp,adjusted}) \times \alpha_{sp}) \quad (23)$$

where $w_{stem,sp}$ (m) and $h_{stem,sp}$ (m) are the width and the height of the stem, respectively, $w_{blade,sp}$ is the width of the blade (m) and α_{sp} is the average number of blades per stem. The frontal area of each tiller is represented as a disk on a 1-mm resolution grid, with the stem at the center and a radius equal to the square root of the frontal area divided by π (Figure 3). All the cells in the disk are considered fully vegetated (i.e., value of 1). Figure 3 also highlights the effect of wind on the frontal area of a tiller for each species. Under no wind (Figure 3, left panel), *A. arenaria*, *A. breviligulata*, and *L. mollis* have a frontal area of 10.2 $\times$ 10^3 mm^2 (Figure 3a), 18.8 $\times$ 10^3 mm^2 (Figure 3c), and 40.6 $\times$ 10^3 mm^2 (Figure 3e), respectively. Under strong wind speeds (i.e., 15 m/s, Figure 3, right panel) their frontal areas are reduced to 3.6 $\times$ 10^3 mm^2 (Figure 3b), 6.3 $\times$ 10^3 mm^2 (Figure 3d) and 8.3 $\times$ 10^3 mm^2 (Figure 3f), respectively. This approach allows vegetation cells to be placed precisely on a high-resolution grid according to the morphological and physical (i.e., blade flexibility) characteristics of each species (Figure 4a). Finally, the 1-mm resolution grid with the vegetation is upscaled to a resolution suitable for the numerical model by computing the vegetation cover (from 0 to 1) in each upscaled (0.05 m for the case of this study) cell (Figure 4b). With this new approach, in the shear stress partitioning model developed by Okin (2008, Equation 13), the height of the canopy h (m) is computed from the stem height $h_{stem,sp}$ (m), the adjusted blade height $h_{blade,sp,adjusted}$ (m) and the vegetation cover in each upscaled cell ρ_{veg} as: $h = (h_{stem,sp} + h_{blade,sp,adjusted})\sqrt{\rho_{veg}}$.

2.2.4. Simulation Settings

We represented the wind tunnel experiment in the AeoLiS model as a horizontal grid ranging from 0 to 7.3 m in the x direction and from 0 to 1 m in the y direction with a resolution of 0.05 m. The wind speeds used in the

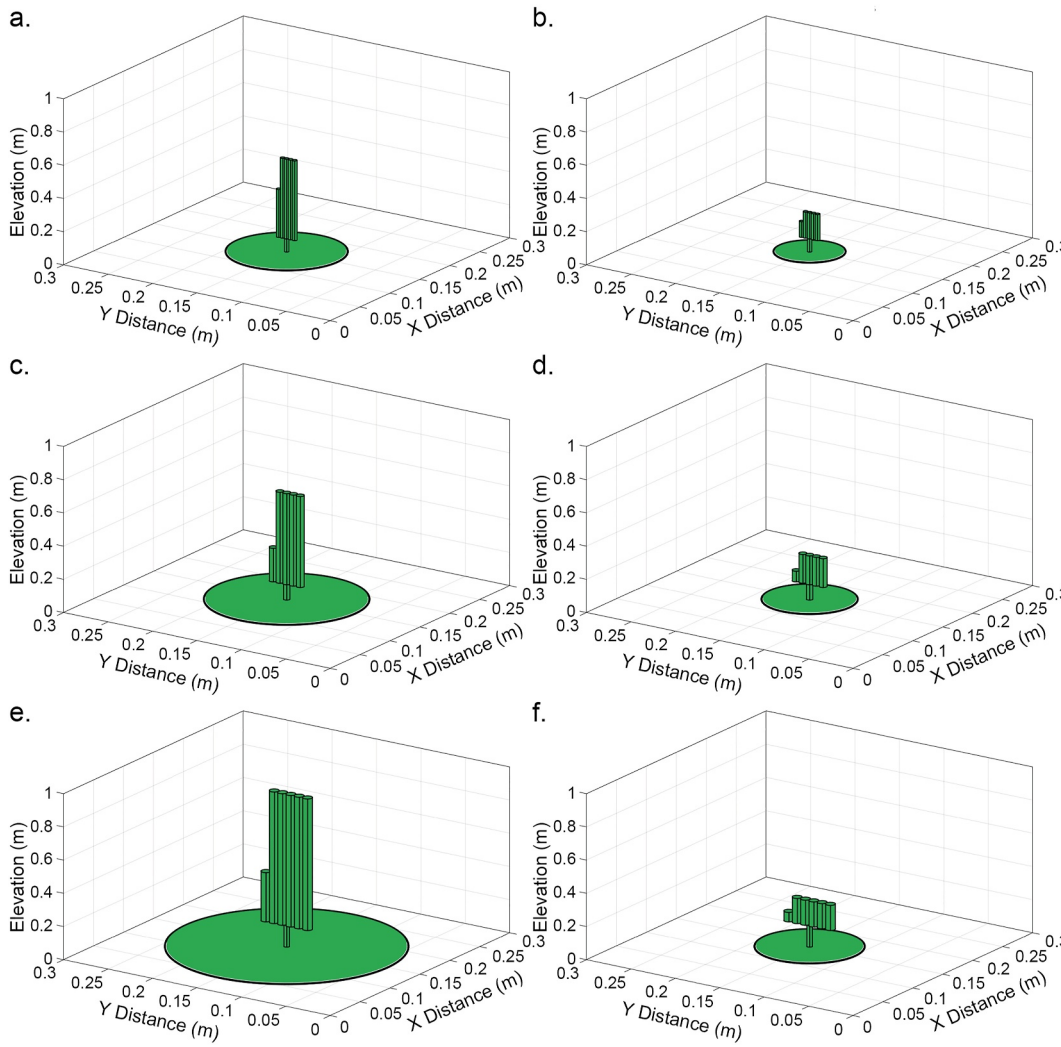

Figure 3. Estimation of the frontal areas of the stem and the blades (vertical) and their projected area as a disk for (a–b) European beachgrass *Ammophila arenaria*, (c–d) American beachgrass *Ammophila breviligulata* and (e–f) native American dune grass *Leymus mollis* under two wind speeds. Wind speeds are equal to 0 m/s (left panel) and 15 m/s (right panel).

simulations were extracted from the tunnel's upwind wind sensors (Figure S3a in Supporting Information S1). Based on the upwind measurements, the low wind speed was 5.97 m/s, and the high wind speed was 9.58 m/s. Mirroring the experimental runs, the simulation runs were 4,800 s for the low wind speed experiments and 1,200 s for the high wind speed experiments. A one m wide and 0.025 m deep layer of sand was implemented in the upwind region of the domain grid covering the distance from $x = 0$ m to $x = 3.4$ m. The wind tunnel experiment used sand from Oregon beaches with a median grain size of 0.24 mm, which we adopted in our model using a single grain size bin of 0.24 mm. For each species and each tiller density within the experimental boxes (see Supporting Information S1), a 1-m^2 vegetated grid with a resolution of 1 mm was created. Random positions within the vegetated grid were generated until the experimental tiller density for each treatment in the boxes was reached (e.g., Figure 4a), as we did not have information about the distribution of tillers within the boxes. Vegetated grids were then used in the model as described in Section 2.2.3. In the shear stress partitioning model developed by Okin (2008), the value of the shear stress recovery-related coefficient, C_1, was set as the default value (i.e., 4.8), and a range of R_0 coefficient values from 0 to 1 in steps of 0.01 were tested. A total of 5,400 test cases were performed (3 species × 2 wind speeds × 9 tiller densities x 100 R_0 coefficient values) following the model process flow chart in Figure 5.

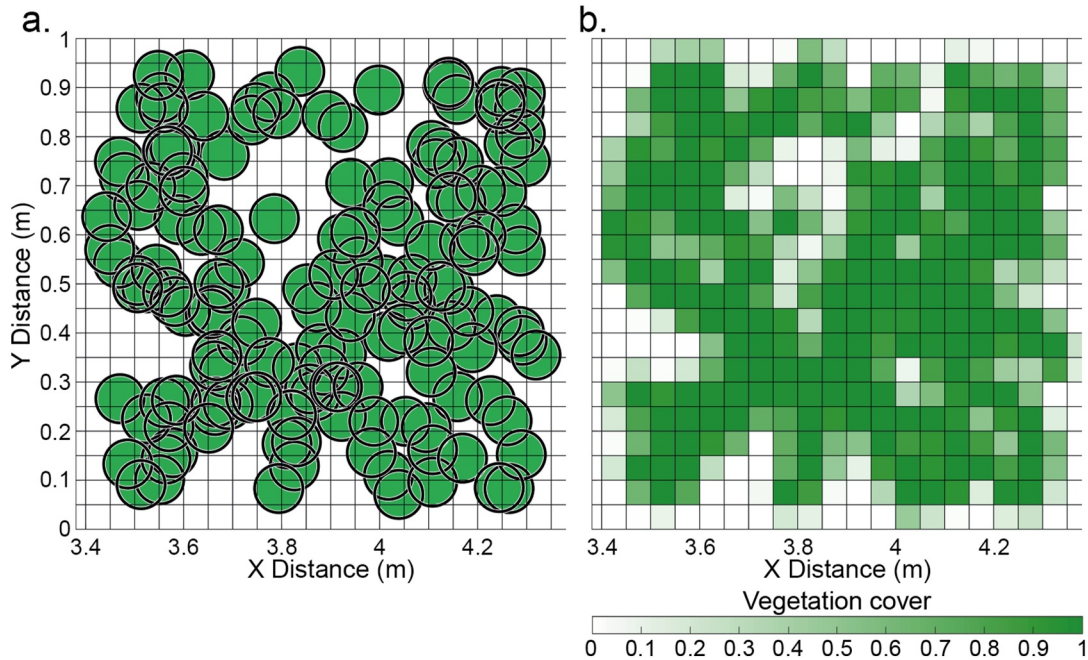

Figure 4. (a) Estimation of the projected areas of tillers of *Ammophila arenaria* with a wind speed of 5.97 m/s in a 1-m^2 grid (tiller density equals 149 tillers/m^2) with a resolution of 0.001 m, (b) Representation of the same vegetation grid upscaled to a 0.05 m resolution grid. The color bar indicates the vegetation cover.

2.3. Model Calibration

To assess the accuracy of the model, the simulated natural-log of the normalized sand capture efficiency, ln(Ce_{norm}), was computed for each tested R_0 coefficient value and compared to the observed ln(Ce_{norm}) from the wind tunnel experiment. For each case, we selected the R_0 value for which the simulated ln(Ce_{norm}) value was closest to the observed data (Figure S4a in Supporting Information S1). However, for 33% of the cases for *A. breviligulata* and 61% of the cases for *L. mollis* (i.e., under medium and high densities), each of the R_0 coefficient values tested led to an underestimation of the simulated ln(Ce_{norm}) compared with the observed data (Figure S4b in Supporting Information S1). This underestimation was characterized by a very slight linear

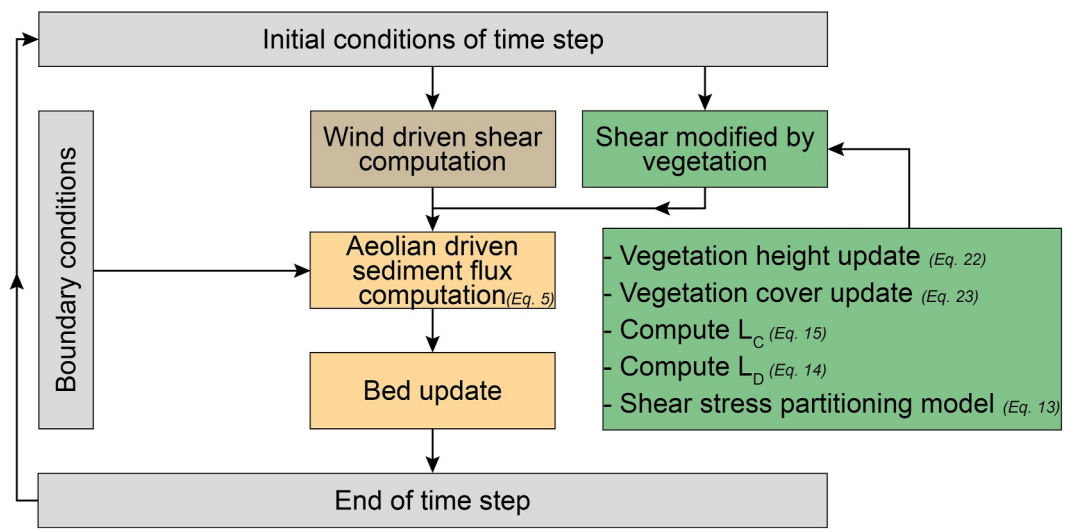

Figure 5. Model process flow chart depicting the order of operations for the implementation of each of the different modules within AeoLiS for one time step of the simulations. The corresponding equations for each process are in Sections 2.2.1–2.2.3.

decrease in the simulated $\ln(Ce_{norm})$ for R_0 coefficients ranging from 0.01 (the smallest value tested) to 0.8, after which the $\ln(Ce_{norm})$ decreased sharply and nonlinearly. In these cases, we calibrated the model (heretofore named "calibrated model" as opposed to the uncorrected model named "initial model") by selecting the R_0 coefficient that gave a simulated $\ln(Ce_{norm})$ of 2% lower than the simulated $\ln(Ce_{norm})$ computed with a $R_0 = 0.01$ (Figure S4b in Supporting Information S1). This choice allowed for the simulated $\ln(Ce_{norm})$ to be the observed $\ln(Ce_{norm})$ and ensured that the chosen "corrected" R_0 coefficients were in line with the uncorrected R_0 coefficients in simulations that did underestimate $\ln(Ce_{norm})$. However, it should be noted that a decrease of 2% of the simulated $\ln(Ce_{norm})$ can lead to a decrease in the accuracy of the calibrated model (Table S3 in Supporting Information S1). As *A. arenaria* did not need to be corrected, the initial model and calibrated R_0 coefficient values were the same.

2.4. Model Performance

The accuracy of the simulated values of $\ln(Ce_{norm})$ compared to the observed values were determined through a variety of statistical analyses. First, we used the Coefficient of Determination (R^2) where a value of 1 implies a strong agreement between the simulated value ($\hat{y}$) and the observed value (y). We also calculated the Willmott Skill score (Equation 24), which is a dimensionless index of agreement, where a value of 1 indicates excellent agreement between the simulated and observed values (Willmott, 1981). Finally, we calculated a Normalized Mean Bias (NMB in %, Equation 25), where a value close to zero indicates total agreement, while positive or negative values characterize overestimation or underestimation, respectively.

$$Skill = 1 - \frac{\sum_{i=1}^{n}\left(\hat{y}_i - y_i\right)^2}{\sum_{i=1}^{n}\left(\left|\hat{y}_i - \bar{y}\right| + \left|y_i - \bar{y}\right|\right)^2} \tag{24}$$

$$NMB = \left\langle \frac{\hat{y} - y}{y} \right\rangle \times 100 \tag{25}$$

3. Results

Results of simulations for sand capture efficiency using the newly proposed species-specific vegetation module in AeoLiS are presented. First, we show metrics of model skill for sand capture efficiency between the wind tunnel observations and the simulations for three cases using the species-specific coefficients with the Okin (2008) model: the "initial" model (model with uncorrected R_0 coefficients, see Section 2.3), the "calibrated" model (model with corrected R_0 coefficient, see Section 2.3), and a "quadratic" curve fit model to the corrected R_0 coefficients that can be used for estimating R_0 for any tiller density at low and high wind speeds. Recall, in the Okin (2008) shear coupler formulation, R_0 characterizes the shear stress reduction due to the presence of vegetation. We call the results of the final quadratic fit model the "species-specific" model, which is used for comparison to the standard model. This version of the model includes a 0.32 default value for the R_0 coefficient and does not include the deposition lag length or the relative blade height. We present a case study of bedforms resulting from the newly proposed species-specific model and the standard model using a constant and a variable species-specific field determined tiller density.

3.1. Calibrated Model

For all three dune grass species, the calibrated model (red data points) showed excellent agreement with the observed data (gray data points) for the metric of sand capture efficiency, $\ln(Ce_{norm})$ (Figures 6a–6c, Table 1). The simulated $\ln(Ce_{norm})$ data for *Ammophila arenaria* agreed well with the measured sand capture efficiencies for all tiller densities and wind speeds (Figure 6a, Table 1). The calibrated R_0 coefficients are between 0.81 and 0.99; the coefficient decreases with increasing tiller density and R_0 is observed to be higher at lower wind speeds (Figure 6d). For *A. breviligulata*, the simulated and observed $\ln(Ce_{norm})$ also have excellent agreement (Table 1). The simulated $\ln(Ce_{norm})$ values agreed for the low and medium tiller densities under both wind speeds, while the high tiller densities were slightly underestimated by the model (Figure 6b). Finally, for *Leymus mollis*, the simulated $\ln(Ce_{norm})$ values that replicated the experimental values at both wind speeds agreed only for the low tiller densities (Figure 6c, Table 1).

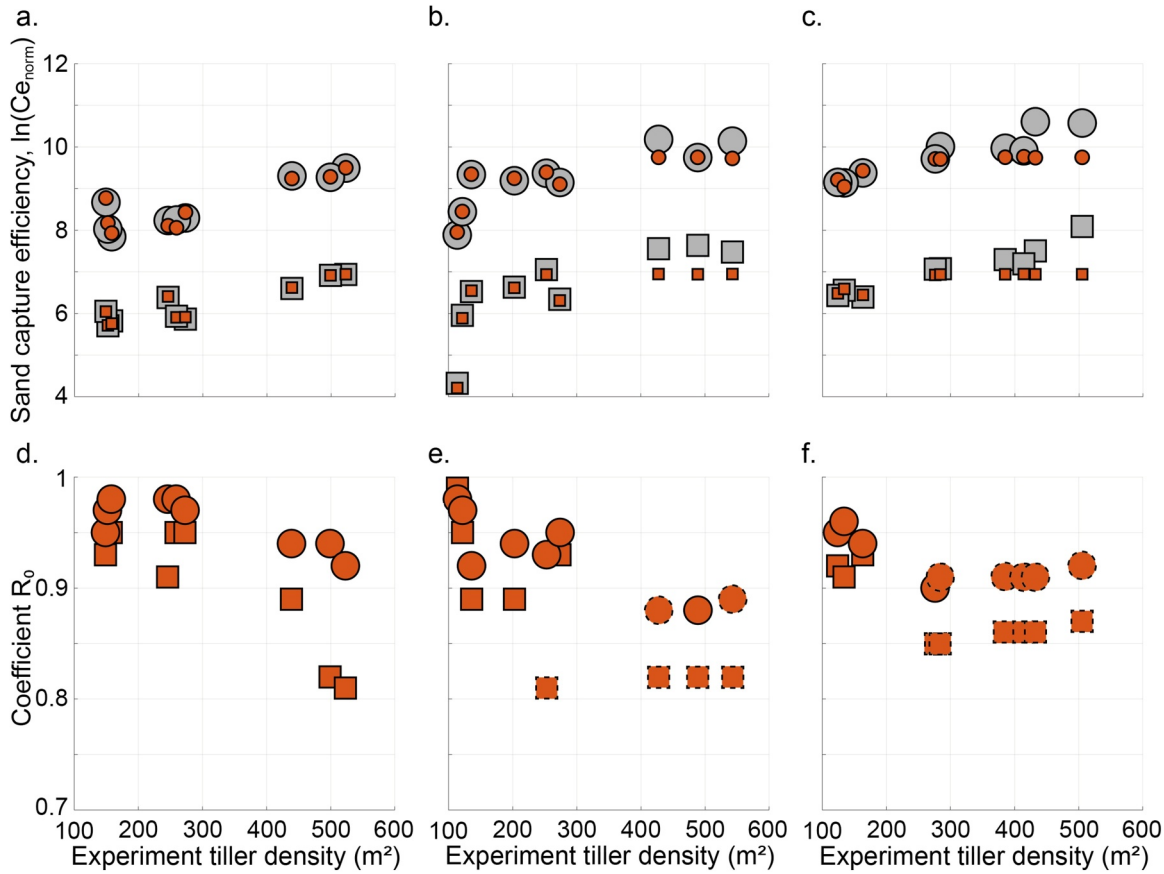

Figure 6. Sand capture efficiency ln(Ce_{norm}) (top row) and R_0 coefficient values (bottom row) as a function of tiller density for (a) and (d) European beachgrass *Ammophila arenaria*, (b) and (e) American beachgrass *A. breviligulata* and (c) and (f) native dune grass *Leymus mollis*. Circles and squares are for low and high wind speeds, respectively. In panels (a)–(c) gray and red colors are for observed and calibrated simulations, respectively. In panels (d)–(f) points with a black dotted outline represent cases where the R_0 coefficient value was corrected, which corresponds to 33% of the cases for *A. breviligulata* and 61% of the cases for *L. mollis*.

The calibrated models for *A. breviligulata* and *L. mollis* are slightly less accurate than the initial models for these two species because a portion of the modeled sand capture efficiencies had to be corrected by reducing the ln (Ce_{norm}) by roughly 2% in order to increase the R_0 coefficient (Table 1, see details in Section 2.3 and Table S3 in Supporting Information S1). For *A. breviligulata,* most high-density tiller treatments were corrected for both wind speeds. The calibrated R_0 coefficient values range from 0.81 to 0.99, decrease with increasing tiller density, and are higher at lower wind speeds (Figure 6e). Additionally, for *L. mollis*, the model underestimates the simulated ln (Ce_{norm}) values for most of the medium and high tiller density cases (Figure 6c). Thus, corrections were made leading to calibrated R_0 coefficient values between 0.86 and 0.96, which decrease with increasing tiller density and are higher at lower wind speeds (Figure 6f).

3.2. Relationship Between R_0, Wind Speed, and Tiller Density

To use the model over a wider range of tiller densities, R_0 coefficient values were interpolated/extrapolated as a function of tiller density, wind speed, and grass species for implementation into the AeoLiS model. We used a quadratic equation to describe the relationships between R_0 and the tiller density (d_{veg}), and we performed this fit for each species and each wind speed. The form of the relationship is given as

$$R_0 = a + b \times d_{veg} + c \times d_{veg}^2 \quad (26)$$

where a, b and c are coefficients listed in Table S4 in Supporting Information S1 and the relationships are shown in Figures 7d–7f. The quadratic relation was highly accurate at explaining the variability in the calibrated R_0

Table 1
Statistical Results for the Relationship Between the Simulated and Observed Species-Specific Sand Capture Efficiency, ln(Ce_{norm}) for the Three Dune Grass Species Combined Using Their Respective R_0 Coefficients (All Species) and Separated by Species (Ammophila arenaria, A. breviligulata, and Leymus mollis)

Sand capture efficiency, ln(Ce_{norm})				
Species	Model	R^2	Skill	NMB (%)
All species	Initial	0.98	0.99	−1.07
	Calibrated	0.97	0.99	−1.65
	Quadratic	0.92	0.98	−0.76
A. arenaria	Initial	0.99	0.99	0.10
	Calibrated	0.99	0.99	0.10
	Quadratic	0.95	0.98	−0.11
A. breviligulata	Initial	0.99	0.99	−1.43
	Calibrated	0.98	0.99	−2.04
	Quadratic	0.87	0.96	0.82
L. mollis	Initial	0.96	0.99	−1.87
	Calibrated	0.94	0.98	−3.01
	Quadratic	0.92	0.97	−3.00

Note. The model column distinguishes if the R_0 coefficient computed was uncorrected (i.e., initial model), corrected (i.e., calibrated model), or computed using the quadratic equation.

coefficient values (Table 2). The computed R_0 coefficient for each species and wind speed were then used in the AeoLiS model to compute a new simulated ln(Ce_{norm}), which agrees with the observed sand capture efficiency for all species (Figures 7a–7c, Table 1). The simulated values of ln(Ce_{norm}) are underestimated mainly for *A. breviligulata* (high tiller densities under both wind speeds, Figure 7b) and *L. mollis* (medium and high tiller densities under both wind speeds, Figure 7c). Compared with the calibrated model results, the accuracy of the simulated ln(Ce_{norm}) values for *A. breviligulata* decreased the most, while the accuracy for *A. arenaria* and *L. mollis* were nearly the same for both the calibrated model simulations and the quadratic relationship simulations (Table 1). The R_0 coefficient computed by the quadratic relationship for each species ranges from 0.82 to 0.97 for *A. arenaria* (Figure 7d), 0.81 to 0.96 for *A. breviligulata* (Figure 7e) and 0.85 to 0.95 for *L. mollis* (Figure 7f). These values for the R_0 coefficient were similar to the calibrated values except for the low and medium tiller densities under both wind speeds for *A. breviligulata*, which remain within a very narrow range (0.03 on average, Figure 7e).

3.3. Simulated Bedforms Using the New Approach for Representing Vegetation Species Characteristics in AeoLiS

In order to assess the implementation of species-specific sand capture in the AeoLiS model, we simulated the bedform building process for each species. Simulations, including the deposition lag length (L_D, Figure S1 in Supporting Information S1) and the values of the R_0 coefficient computed by the species-specific quadratic equation (Equation 26) now referred to as the "species-specific model," were performed by following the computational steps outlined in the flow chart (Figure 5). In addition, simulations with the standard AeoLiS model, which does not include the deposition lag length, the relative blade height, and has a default value of 0.32 for the R_0 coefficient, were performed for comparison. Our simulations included two tiller densities and two wind speeds (Figure 8). The tiller densities were either equal for all species (i.e., 125 tiller/m^2) or species-specific from field measurements (i.e., 222 tiller/m^2 for *A. arenaria*, 124 tiller/m^2 for *A. breviligulata* and 41 tiller/m^2 for *L. mollis*, from Appendix A in Zarnetske et al., 2012). Regardless of model (i.e., standard model and species-specific model), the tiller density or plant species, sand deposition was greater at higher wind speeds (Figures 8b and 8d) than at lower wind speeds (Figures 8a and 8c).

Simulations with the standard AeoLiS model (dashed lines on Figure 8) result in bedforms with their stoss side initiating at the beginning of the vegetation patch with crest heights more than twice as high and bedform widths about 30% wider on average compared to the species-specific model (solid lines on Figure 8). In addition, in each case using the standard AeoLiS model, the bedforms are almost identical, not showing any clear distinction between species. Any differences between the standard AeoLiS model simulations can be attributed to simply changes in field realistic vegetation density, which was implemented as an initial condition for all simulations and specific to each species.

The simulations with the species-specific model (solid lines on Figure 8) with equal (125 tillers m^2) tiller densities show that the native *L. mollis* traps more sand and builds the highest and widest bedform compared to the non-native *A. arenaria*, which has the lowest sand deposition and longest deposition lag length (Figures 8a and 8b, and Table 3). *A. breviligulata* has intermediate sand deposition and lag length. The tiller field density simulations show the opposite result with *A. arenaria* having the shortest deposition lag length, followed by *A. breviligulata*, and then *L. mollis*, which has a deposition lag length that is at least twice as long as the other two species (Table 3). For the low wind speed, the average sand deposition for *A. arenaria* and *A. breviligulata* are similar, whereas the average sand deposition for *L. mollis* is lower (Figure 8c and Table 3). For the high wind speed, *A. arenaria* builds a taller and steeper bedform, while *A. breviligulata* builds a shorter and wider bedform. The bedform simulated for *L. mollis* remains much smaller compared to the two other plant species (Figure 8d and Table 3).

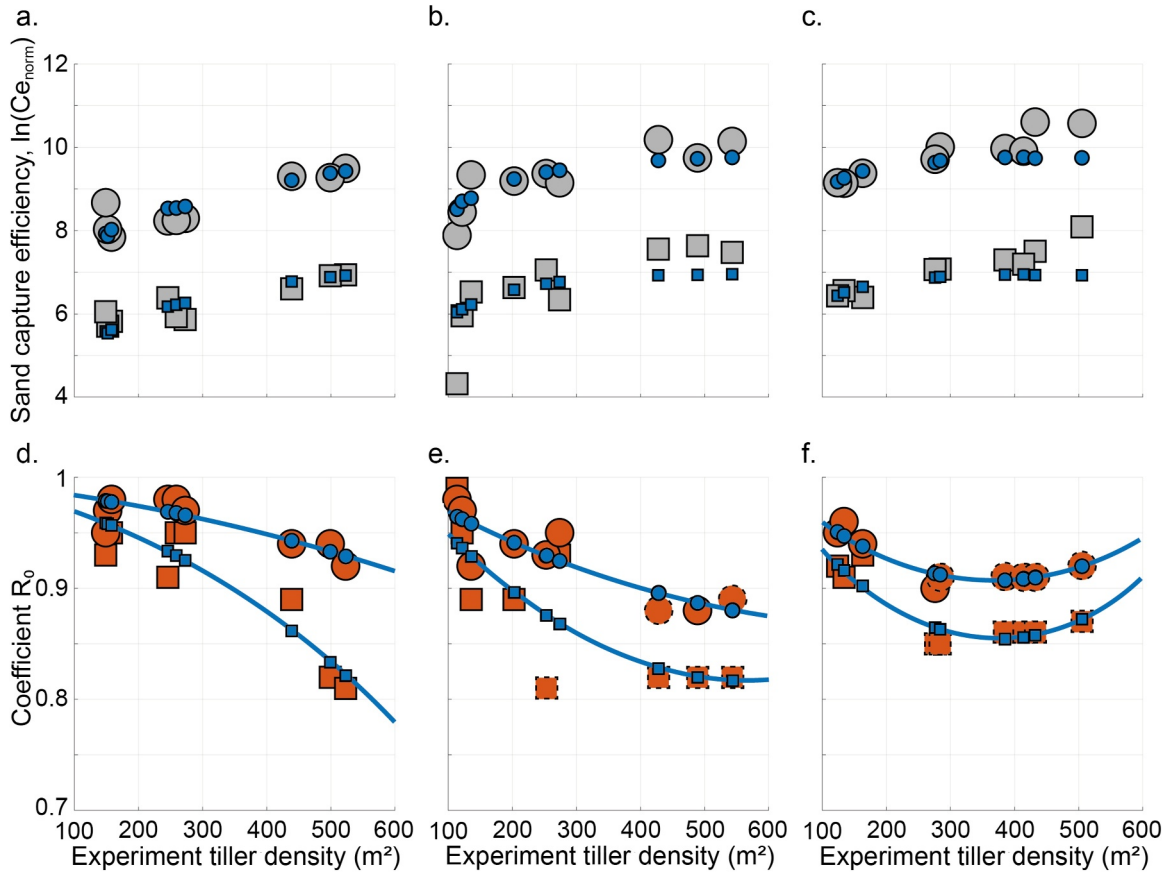

Figure 7. Observed and simulated sand capture efficiency ($\ln(Ce_{norm})$) (top row); gray points show wind tunnel observations and blue points show simulations from the species specific-model using the quadratic equation. Estimated R_0 coefficient (bottom row); red points show the calibrated model, blue points show the quadratic fit, and red points with a black dotted outline represent cases where the R_0 value has been corrected. Simulations are a function of species and wind speed: (a) and (d) European beachgrass *Ammophila arenaria*, (b) and (e) American beachgrass *A. breviligulata* and (c) and (f) native dune grass *Leymus mollis*. Squares represent high wind speeds and circles represent low wind speeds. Each species is fitted with a quadratic equation for each wind speed (blue lines).

4. Discussion

The objective of this study was to develop a new approach to incorporate the species-specific characteristics of vegetation into the process-based aeolian transport and dune morphologic change model AeoLiS. Species-specific characteristics of three dune grass species (i.e., *Ammophila arenaria*, *A. breviligulata,* and *Leymus mollis* from the US Pacific Northwest) were introduced into the model in three ways. First, plant characteristics were used to modify the deposition lag length in the shear stress coupler. Second, the coefficients in the shear stress coupler were calibrated with wind tunnel data by computing the sand capture efficiency of the three plant species for various tiller densities and wind speeds. Third, a species-specific model was developed to relate the calibrated coefficients to tiller density and wind speed for each species using a quadratic equation. Finally, the species-specific model was used to produce dune bedforms with shapes similar to those from experimental and field observations.

Table 2
Assessment of Accuracy for R_0 Coefficients Computed Using the Quadratic Relationship Compared to the Calibrated R_0 Coefficient for All Species Combined, Ammophila arenaria, A. breviligulata, and Leymus mollis

Species	R^2	Skill	NMB (%)
All species	0.83	0.95	0.07
A. arenaria	0.88	0.97	0.19
A. breviligulata	0.73	0.92	0.05
L. mollis	0.92	0.98	−0.04

4.1. AeoLis Vegetation Module Performance

We have provided three key improvements to the AeoLiS model: (a) A detailed estimate of the planar area of vegetation based on species-specific morphological characteristics (upscaling approach shown in Section 2.2.3), (b) Modification of the Okin (2008) shear coupler to include planar area estimates for implementing shear reduction through varying tiller density canopies of vegetation (proposed quadratic relation for R_0), and (c)

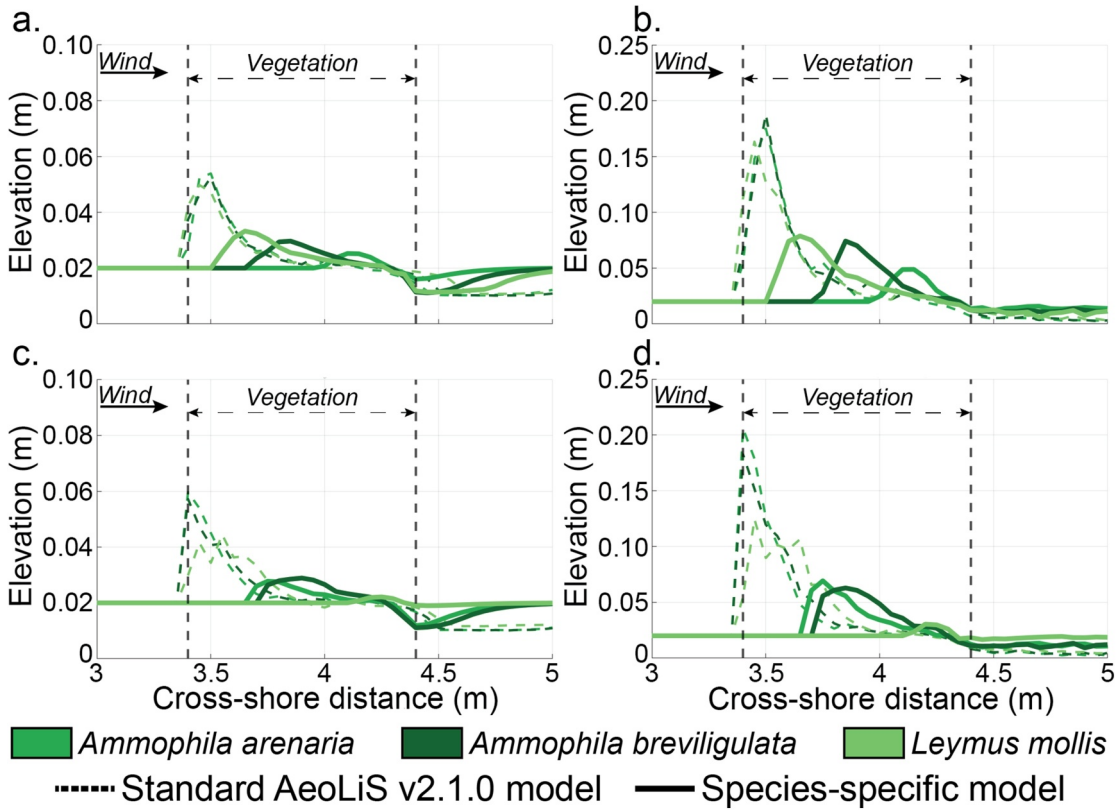

Figure 8. Simulated width-averaged along-tunnel profiles with the standard AeoLiS model (dashed line) and the species-specific model (solid line) for *Ammophila arenaria*, *A. breviligulata* and *Leymus mollis*. The R_0 coefficient value is computed using Equation 26 with (a) low wind speed and equal tiller densities, (b) high wind speed and equal tiller densities, (c) low wind speed and species-specific field tiller densities and (d) high wind speed and species-specific field tiller densities. The vertical axis is different between low wind speed (left panel) and high wind speed (right panel).

Implementing a parameterization for the modified shear coupler starting at the deposition lag length position (L_D, following Dickey et al., 2023).

Using the species-specific model, our results were consistent with the main conclusions of Zarnetske et al. (2012), whereas the standard AeoLiS model produced inconsistent results. With the species-specific model, regardless of the grass species, the simulated sand capture efficiency ($\ln(Ce_{norm})$) was higher for low wind speeds and higher tiller densities. The simulated $\ln(Ce_{norm})$ was highest for *L. mollis*, followed by *A. breviligulata*, and *A. arenaria*. The tiller characteristics (e.g., tiller width, blade per tiller, tiller length and biomass) for *L. mollis* created greater surface area, favoring more sand deposition compared to *A. breviligulata* and *A. arenaria,* which have lower surface areas and less sand deposition.

We found that tiller morphology and tiller density play a major role in sand capture efficiency. In particular, we found that for the same tiller density (125 tiller/m^2, Figure 8), the morphological characteristics of the vegetation are important, and *L. mollis* traps more sand than the two *Ammophila* species due to its larger frontal area. For both wind speeds, the simulated bedforms of *L. mollis* were taller and wider, and its deposition lag length was shorter. Given its thinner tillers, *A. arenaria* had low sand deposition, whereas *A. breviligulata*, with its intermediate tiller size, was positioned between the other two species. Under field tiller densities however, both *Ammophila* grass species reach higher tiller densities (*A. arenaria* tillers/m^2 ± 1SE, variance/mean ratio: 222 ± 15, max: 373 ± 32, absolute min: 1/m^2, and for *A. breviligulata* tillers/m^2 ± 1SE, variance/mean ratio: 124 ± 13, max: 294 ± 25, absolute min: 1/m^2) than *L. mollis* (tillers/m^2 ± 1SE, variance/mean ratio: 41 ± 4, max: 66 ± 8, absolute min: 1/m^2) (Zarnetske et al., 2012). Correspondingly, the sand capture in the simulations was 9 times greater for the *Ammophila* grass species than for *L. mollis*. The Zarnetske et al. (2012) experiments found that the sand capture of the two *Ammophila* species was 5 times greater than *L. mollis*.

Table 3

Model Inputs and Output Characteristics for Bedforms Simulated With the Standard AeoLiS Model (i.e., R_0 Coefficient Equal to 0.32, Written in Bold) and the Species-Specific Model (i.e., R_0 Coefficient Computed by Quadratic Equations, See Section 3.2) for Ammophila arenaria, A. breviligulata, and Leymus mollis Under Two Tiller Densities Conditions (i.e., a Constant 125 Tillers/m^2 and a Variable Species-Specific Field Determined Tiller Density) and Two Wind Speeds

Species	Tiller density (shoot/m^2)	Wind speed (m/s)	R_0 value	Deposition lag length (cm)	Bedform height (cm)	Bedform width (cm)
A. arenaria	125	5.97	0.98	55	0.54	35
A. arenaria	**125**	**5.97**	**0.32**	**0**	**3.39**	**55**
A. breviligulata	125	5.97	0.96	25	0.96	65
A. breviligulata	**125**	**5.97**	**0.32**	**0**	**3.25**	**85**
L. mollis	125	5.97	0.95	10	1.33	76
L. mollis	**125**	**5.97**	**0.32**	**0**	**2.97**	**70**
A. arenaria	125	9.58	0.96	55	3.03	40
A. arenaria	**125**	**9.58**	**0.32**	**0**	**15.48**	**55**
A. breviligulata	125	9.58	0.93	30	5.42	65
A. breviligulata	**125**	**9.58**	**0.32**	**0**	**16.77**	**70**
L. mollis	125	9.58	0.92	10	5.88	76
L. mollis	**125**	**9.58**	**0.32**	**0**	**14.32**	**70**
A. arenaria	222	5.97	0.97	25	0.78	61
A. arenaria	**222**	**5.97**	**0.32**	**0**	**3.97**	**60**
A. breviligulata	124	5.97	0.96	30	0.88	56
A. breviligulata	**124**	**5.97**	**0.32**	**0**	**3.72**	**55**
L. mollis	41	5.97	0.98	70	0.10	25
L. mollis	**41**	**5.97**	**0.32**	**0**	**2.44**	**55**
A. arenaria	222	9.58	0.94	25	4.93	65
A. arenaria	**222**	**9.58**	**0.32**	**0**	**18.57**	**75**
A. breviligulata	124	9.58	0.93	30	4.28	60
A. breviligulata	**124**	**9.58**	**0.32**	**0**	**16.24**	**70**
L. mollis	41	9.58	0.97	70	1.04	24
L. mollis	**41**	**9.58**	**0.32**	**0**	**10.44**	**65**

Additionally, in the field, the growth form of the three grass species plays an important role in sand deposition (Hacker et al., 2012; Reijers et al., 2019), and the field tiller densities used in our study better capture the variability observed among quadrats (i.e., variance/mean ratio, Zarnetske et al., 2012), making them more realistic in reflecting species-specific growth forms. The vertical growth form and high shoot density of *A. arenaria* lead to the development of high and narrow dunes, the lateral growth form and lower shoot density of *A. breviligulata* lead to the development of shorter and wider dunes, while *L. mollis* builds even shorter and wider dunes due to its lateral growth form and very low shoot density (Hacker et al., 2012; Zarnetske et al., 2012). We observe similar dune morphology in the simulated bedforms using the planar area modifications within AeoLiS (Figure 8). For example, the simulated bedform of *A. arenaria* is taller and narrower than the bedform of *A. breviligulata*, and the *L. mollis* bedform is much shorter and wider under field realistic tiller densities with high wind speeds. In comparison, even though the standard AeoLiS model simulated larger bedforms for high wind speeds, the simulated bedforms were (a) nearly identical for all three grass species under the constant density conditions (i.e., 125 tiller/m^2), (b) nearly identical for both *Ammophila* species and slightly smaller for *L. mollis* under the field realistic tiller densities. These results highlight the inconsistencies between the standard AeoLiS model and the results from the wind tunnel experiment of Zarnetske et al. (2012). Despite some limitations (see Section 4.2), the modifications of AeoLiS allow for realistic simulations of species-specific sand deposition and the resulting developed bedforms. Simulation skill compares well with wind tunnel experimental data (Zarnetske et al., 2012) and is consistent with expectations from field observations (Hacker et al., 2012).

4.2. Limitations of Model Parameterization

Despite the agreement between the simulations and experimental results, there are some limitations to our methods. First, for high tiller densities, it is possible for the grid to become saturated and completely covered with vegetation, obscuring differences between plant species. For a 1-m^2 grid, it is not possible to reach 100% cover in every cell, as vegetation is implemented as a disc, so grid contours will always remain somewhat sparsely vegetated. In the absence of wind and thus blade bending, 90% of the horizontal grid will be covered by vegetation at 550 tillers for *A. arenaria*, 425 tillers for *A. breviligulata* and 250 tillers for *L. mollis*. With increased wind speed, the frontal tiller area decreases and therefore the applied planar surface decreases (e.g., at a wind speed of 10 m/s, at least 950 tillers are needed to cover 90% of the horizontal grid for each species). However, these high densities are rarely found under field conditions (Zarnetske et al., 2012) and thus would not normally be used in realistic simulations.

Another limitation of the model was the calibration of the R_0 coefficient. For 33% of *A. breviligulata* cases (mainly for the high tiller densities for both wind speeds) and 61% of *L. mollis* cases (mainly for the medium and high tiller densities for both wind speeds), there was an underestimate of the simulated $\ln(Ce_{\text{norm}})$ compared to experimental observations for all R_0 values. For these cases, although the initial amount of sand upwind of the vegetation was the same for the wind tunnel experiment and the simulations, the model overestimated the volume of sand removed from the upwind zone. According to Equation 1, this overestimation leads to an increase in the value of s_{in} (the difference between the initial and final upwind sand mass) and therefore decreases the value of Ce (the sand capture efficiency) and thus $\ln(Ce_{\text{norm}})$. To address this issue in future simulations, it is possible to adjust the constant C in the transport equation (Equation 5) to reduce the amount of sand removed from the upwind zone, which would increase the sand capture efficiency (Ce). However, this approach would require case-by-case calibration, making it more difficult to replicate and apply the model broadly across different conditions.

We also found that the quantity of sand removed upwind of the vegetation in the wind tunnel varied with respect to plant species and tiller densities under both wind speeds (Figure S3b in Supporting Information S1) and was negatively related to tiller density (the difference (Δ) in sand removed between low and high tiller densities reached $\Delta = 22.6$ kg for *A. arenaria*, $\Delta = 27.9$ kg for *A. breviligulata* and $\Delta = 45$ kg for *L. mollis* for high wind speeds and $\Delta = 14.6$ kg for *A. arenaria*, $\Delta = 35.1$ kg for *A. breviligulata* and $\Delta = 16.1$ for *L. mollis* at low wind speeds). The lowest variation of sand removed upwind of the vegetation across all the experimental runs and for both wind speeds was measured for *A. arenaria*, while *L. mollis* had the largest variation. These differences might be explained by back flow conditions, in which there is a zone of slowdown upwind of structures such as sand fences or vegetation (Hesp et al., 2019; Mayaud et al., 2016; Mayaud & Webb, 2017) that can extend up to three times the height of the structure (Zhang et al., 2010). This back flow effect may explain the variability in sand removal in the wind tunnel experiment, but we are unable to verify this hypothesis given that there was only one wind sensor upwind of the vegetation (Figure S3a in Supporting Information S1).

Finally, the wind tunnel experiment was performed under only two wind speeds. Miri et al. (2017, 2018, 2019) carried out a series of wind tunnel experiments to assess the flow dynamics and sediment transport for two plant species (*Cosmos bipinnatus* a medium-sized herbaceous plant and *Ligustrum lucidum* a broadleaf tree) under three densities and several wind speeds. They found that frontal area and lateral cover decreased nonlinearly with increasing wind speed. Stiffer plants can maintain their frontal area for a range of wind speeds until a threshold is reached and the frontal area declines (Gillies et al., 2002; Middleton et al., 1984; Vollsinger et al., 2005). Given this non-linearity, it is recommended that multiple wind speeds are used to parameterize species-specific frontal area for the computation of R_0.

4.3. Future Model Improvements

In this study, a new approach was developed to consider dune grass species-specific characteristics on sand transport and sand deposition. While this approach showed promising simulation results, there is still potential for improvement. The effect of vegetation on shear velocity and sand transport was simulated using the shear stress coupler developed by Okin (2008). At this point, this formulation only allows for 1D wind-vegetation interactions on the lee side of the vegetation (i.e., air flow deceleration and acceleration) and cannot simulate the development of variable flow regimes around the plant. Indeed, as the wind approaches the vegetation, the layer of air between the surface and the top of the vegetation slows down and separates into several upwind regimes. The flow is compressed and forced around the vegetation, creating a zone of eddy acceleration above and around the plants,

potentially eroding sediment on the surface. The flow also passes through the vegetation and decelerates, forming a zone of low velocity in the sheltered area favoring sediment deposition. In some cases, the adverse pressure gradient causes the velocity to decrease so much that the boundary layer can reverse and separate. A turbulent mixing layer develops above and leeward of the slow-speed zone from a thin layer at the top of the vegetation and eventually reaches the surface. Finally, the mixing zone merges and equilibrates as the airflow recovers and becomes equivalent to the upwind profile (Fu et al., 2019; Hesp & Smyth, 2017; Judd et al., 1996; Mayaud et al., 2016; Mayaud & Webb, 2017; Wolfe & Nickling, 1993). To overcome the limitations of Okin's model, Leenders et al. (2011) has developed a 2D wind-blown sediment transport model to spatially account for sediment transport in regions around the vegetative element through incorporating wind reduction and acceleration zones. Implementation of the Leenders et al. (2011) modification or other more complex shear coupling approaches into the AeoLiS model could provide a better characterization of flow and associated sand transport in 2D at the scale of vegetation patches. However, it should be noted that while the implementation of more complex physical processes and approaches in the model could allow simulations to be solved in fine detail, it could also limit the model's application to simulating sediment transport over long time scales.

Also, few studies have used species-specific parameterization to model dune evolution. This would require measurements of sand transport associated with different species at varying densities and wind speeds in a wind tunnel setting or controlled field conditions. However, this type of research is rare. Charbonneau et al. (2021) performed a wind tunnel experiment involving three US East coast foredune pioneer plant species (i.e., *A. breviligulata*, *Panicum amarum*, and *Carex kobomugi*) to understand the role of the intraspecific variation in vegetation morphology, density, and configuration impacting geomorphological processes in aeolian beach-dune systems. Despite the two densities tested, the experiment used only one wind speed, which likely limits the parameterization of the model. Other studies have used artificial plants to mimic the characteristics of live plants. For example, Cheng et al. (2018) conducted a series of wind tunnel experiments to simulate the average airflow speed and turbulence intensities on the lee side of eight single plants made in plastic under eight different wind speeds. Hesp et al. (2019) used an artificial plastic vegetation canopy in an open circuit wind tunnel to investigate the flow dynamics within and above the canopy and the sand transport associated under two wind speeds and various densities. Results from these studies could be used to improve aeolian sediment transport models and the consideration of species-specific characteristics of wind flow and sand transport.

Moving from controlled experimental cases to realistic field applications is a crucial next step in the development of coastal dune models. One of the main challenges lies in translating field data of vegetation, such as plant density and spatial distribution, into inputs suitable for the model. The new approach developed in this study seeks to include realistic plant density, morphology, and growth form characteristics of the three dune grass species to more accurately determine differences in sand capture efficiency and dune building capabilities. However, we found that under high plant densities, the model can underestimate sand capture, potentially leading to inaccurate estimates of dune growth. For example, field-realistic tiller densities for *A. breviligulata* and *L. mollis* are on average 124 and 41 tillers/m^2, respectively (Zarnetske et al., 2012). The underestimation of the sand capture efficiency is only evident at higher tiller densities (i.e., 400 tillers/m^2 for *A. breviligulata* and 250 tillers/m^2 for *L. mollis*), which are uncommon in natural field conditions. As a result, this limitation should have minimal impact on simulating realistic dune growth. Beyond the tiller density, it is also essential to capture the spatial distribution (i.e., the growth form) of vegetation across the domain, as this can significantly influence sand capture and dune morphology (Biel et al., 2019; Charbonneau et al., 2021; Goldstein et al., 2017; Hacker et al., 2012, 2019; Zarnetske et al., 2012, 2015). For large-scale, realistic simulations, tiller locations and densities can be derived from field surveys (e.g., with quadrats and transects) or remote sensing technologies such as lidar, satellite imagery, multispectral, and hyperspectral imagery (De Giglio et al., 2019; Laporte-Fauret et al., 2020; Marzialetti et al., 2019; Suir et al., 2023). Alternatively, when field data are not available, simulating vegetation dispersion using Lévy-type colonization strategies (Reijers et al., 2019) may provide realistic plant distribution patterns that can be applied in the model.

5. Conclusions

In this study, a new approach to account for species-specific plant characteristics on sand capture efficiency has been implemented and calibrated into a process-based aeolian sediment transport and coastal dune morphologic change model. First, vegetation is implemented in the model depending on the morphological characteristics of each plant species. Then, a coefficient characterizing the effect of vegetation on shear velocity was calibrated

using a wind tunnel experiment involving three species (*Ammophila arenaria*, *A. breviligulata* and *Leymus mollis*) with nine tiller densities under two wind speeds. A species-specific model was developed to relate the coefficient to tiller density and wind speed for each species and simulated the sand capture efficiency of each species with strong agreement. Two sets of model simulations of bedform development were performed, one with the same tiller density and the second with field-realistic tiller densities, both with the standard AeoLiS model and the new species-specific model. For each case, the standard model simulated greater and almost similar bedforms from one species to the next, not consistent with the wind tunnel experiment results. With the species-specific model, under the same density, the species with the largest frontal area (i.e., *L. mollis*) had a higher simulated sand capture efficiency and captured more sediment, aligned with results from the wind tunnel experiment. Under field-realistic tiller densities, *A. arenaria* and *A. breviligulata* had a better sand capture efficiency due to their higher densities with simulated bedforms consistent with field measurements and observations.

Although the proposed approach for implementing species-specific vegetation metrics for sand capture into AeoLiS still needs to be tested under a variety of conditions, our results show promise. Implications of this work include improvements in our ability to assess medium- to long-term evolution of coastal dunes, scales that are relevant for dune management decision making. The new modeling approach will also improve our understanding of coastal dune ecomorphodynamics, which play an essential role in the evolution of coastal dunes, particularly in the context of climate change induced sea-level rise and the recovery from storm impacts.

Data Availability Statement

The data used as a reference for the model calibration in this article are based on the wind tunnel experiment of Zarnetske et al. (2012). Version 2.1.0 of the standard AeoLiS software used for the aeolian sediment transport simulations in this research is preserved at https://github.com/openearth/aeolis-python/tree/v2.1.0 (AeoLiS Development Team, 2023). The version 2.1.0 of the AeoLiS model with the new implementations in the vegetation module and the vegetation grids used in this research are preserved at https://zenodo.org/records/13930739 (Laporte-Fauret et al., 2024).

Acknowledgments
This work was funded by the US Army Corps of Engineers (USACE) Grant W912HZ2120045 and the USACE Coastal Inlets Research Program (CIRP) Coastal Forecasting to Reduce Infrastructure Flooding (CFRIF) program. Additional support was provided by the Cascadia Coastlines and Peoples Hazards Research Hub, NSF Coastlines and People Large-Scale Hub (NSF award number 2103713). We would like to acknowledge Risa Askerooth, Cole Thieme, and Danielle Whalen for measuring the dune grass morphology and growth form.

References

AeoLiS Development Team. (2023). AeoLiS releast (version 2.1.0) [Software]. *GitHub*. Retrieved from https://github.com/openearth/aeolis-python/tree/v2.1.0

Alfieri, L., Feyen, L., Dottori, F., & Bianchi, A. (2015). Ensemble flood risk assessment in Europe under high end climate scenarios. *Global Environmental Change*, *35*, 199–212. https://doi.org/10.1016/j.gloenvcha.2015.09.004

Baas, A. C. (2002). Chaos, fractal sand self-organization in coastal geomorphology: Simulating dune landscapes in vegetated environments. *Geomorphology*, *48*(1–3), 309–328. https://doi.org/10.1016/S0169-555X(02)00187-3

Bagnold, R. A. (1937). The transport of sand by wind. *The Geographical Journal*, *89*(5), 409. https://doi.org/10.2307/1786411

Bagnold, R. A. (1941). *The physics of blown sand and desert dunes* (Vol. 265). Chapman and Hall.

Barbier, E. B., Hacker, S. D., Kennedy, C., Koch, E. W., Stier, A. C., & Silliman, B. R. (2011). The value of estuarine and coastal ecosystem services. *Ecological Monographs*, *81*(2), 169–193. https://doi.org/10.1890/10-1510.1

Barbour, M., Jong, T., & Pavlik, B. (1985). Marine beach and dune plant communities. In B. Chabot & H. Mooney (Eds.), *Physiological ecology of North American plant communities* (pp. 296–322). Chapman & Hall and Methuen.

Belcher, S. E., Jerram, N., & Hunt, J. C. R. (2003). Adjustment of a turbulent boundary layer to a canopy of roughness elements. *Journal of Fluid Mechanics*, *488*, 369–398. https://doi.org/10.1017/S0022112003005019

Biel, R. G., Hacker, S. D., & Ruggiero, P. (2019). Elucidating coastal foredune ecomorphodynamics in the U.S. Pacific Northwest via Bayesian networks. *Journal of Geophysical Research: Earth Surface*, *124*(7), 1919–1938. https://doi.org/10.1029/2018JF004758

Bradley, E. F., & Mulhearn, P. J. (1983). Development of velocity and shear stress distributions in the wake of a porous shelter fence. *Journal of Wind Engineering and Industrial Aerodynamics*, *15*(1–3), 145–156. https://doi.org/10.1016/0167-6105(83)90185-X

Buckley, R. (1987). The effect of sparse vegetation on the transport of dune sand by wind. *Nature*, *325*(6103), 426–428. https://doi.org/10.1038/325426a0

Charbonneau, B. R., Dohner, S. M., Wnek, J. P., Barber, D., Zarnetske, P., & Casper, B. B. (2021). Vegetation effects on coastal foredune initiation: Wind tunnel experiments and field validation for three dune-building plants. *Geomorphology*, *378*, 107594. https://doi.org/10.1016/j.geomorph.2021.107594

Charbonneau, B. R., Wnek, J. P., Langley, J. A., Lee, G., & Balsamo, R. A. (2016). Above vs. belowground plant biomass along a barrier island: Implications for dune stabilization. *Journal of Environmental Management*, *182*, 126–133. https://doi.org/10.1016/j.jenvman.2016.06.032

Cheng, H., Zhang, K., Liu, C., Zou, X., Kang, L., Chen, T., & Fang, Y. (2018). Wind tunnel study of airflow recovery on the lee side of single plants. *Agricultural and Forest Meteorology*, *263*, 362–372. https://doi.org/10.1016/j.agrformet.2018.08.025

Cohn, N., Hoonhout, B., Goldstein, E., De Vries, S., Moore, L., Durán, O., & Ruggiero, P. (2019). Exploring Marine and Aeolian controls on coastal foredune growth using a coupled numerical model. *Journal of Marine Science and Engineering*, *7*(1), 13. https://doi.org/10.3390/jmse7010013

Cohn, N., Ruggiero, P., de Vries, S., & Kaminsky, G. M. (2018). New insights on coastal foredune growth: The relative contributions of marine and aeolian processes. *Geophysical Research Letters*, *45*(10), 4965–4973. https://doi.org/10.1029/2018GL077836

Cooper, J. A. G., Masselink, G., Coco, G., Short, A. D., Castelle, B., Rogers, K., et al. (2020). Sandy beaches can survive sea-level rise. *Nature Climate Change*, *10*(11), 993–995. https://doi.org/10.1038/s41558020-00934-2

De Giglio, M., Greggio, N., Goo, F., Merloni, N., Dubbini, M., & Barbarella, M. (2019). Comparison of pixel-and object-based classification methods of unmanned aerial vehicle data applied to coastal dune vegetation communities: Casal borsetti case study. *Remote Sensing*, *11*, 1416. https://doi.org/10.3390/rs11121416

de Groot, A., Berendse, F., Riksen, M., Baas, A., Slim, P., Dobben, H. V., & Stroosnijder, L. (2011). Modelling coastal dune formation and associated vegetation development. *Geophysical Research Abstracts*, *13*(6), 4959. http://meetingorganizer.copernicus.org/EGU2011/EGU2011-4959.pdf

de Vries, S., Hallin, C., van IJzendoorn, C., van Westen, B., Cohn, N., Strypsteen, G., et al. (2023). AeoLiS (version v2.1.0) [Software]. *4TU Repository*. https://doi.org/10.4121/22215562

de Vries, S., van Thiel de Vries, J. S. M., van Rijn, L. C., Arens, S. M., & Ranasinghe, R. (2014). Aeolian sediment transport in supply limited situations. *Aeolian Research*, *12*, 75–85. https://doi.org/10.1016/j.aeolia.2013.11.005

Dickey, J., Wengrove, M., Cohn, N., Ruggiero, P., & Hacker, S. D. (2023). Observations and modeling of shear stress reduction and sediment flux within sparse dune grass canopies on managed coastal dunes. *Earth Surface Processes and Landforms*, *48*(5), 907–922. https://doi.org/10.1002/esp.5526

Durán, O., & Herrmann, H. J. (2006). Vegetation against dune mobility. *Physical Review Letters*, *97*(18), 188001. https://doi.org/10.1103/PhysRevLett.97.188001

Durán, O., & Moore, L. J. (2013). Vegetation controls on the maximum size of coastal dunes. *Proceedings of the National Academy of Sciences*, *110*(43), 17217–17222. https://doi.org/10.1073/pnas.1307580110

Durán, O., & Moore, L. J. (2015). Barrier island bistability induced by biophysical interactions. *Nature Climate Change*, *5*, 158–162. https://doi.org/10.1038/nclimate2474

Emery, S. M., & Rudgers, J. A. (2014). Biotic and abiotic predictors of ecosystem engineering traits of the dune building grass, *Ammophila breviligulata*. *Ecosphere*, *5*(7), 1–18. https://doi.org/10.1890/ES13-00331.1

Fu, L. T., Fan, Q., & Huang, Z. L. (2019). Wind speed acceleration around a single low solid roughness in atmospheric boundary layer. *Scientific Reports*, *9*(1), 12002. https://doi.org/10.1038/s41598-019-48574-7

Galiforni-Silva, F., Wijnberg, K. M., de Groot, A. V., & Hulscher, S. J. M. H. (2018). The influence of groundwater depth on coastal dune development at sand flats close to inlets. *Ocean Dynamics*, *68*(7), 885–897. https://doi.org/10.1007/s10236-018-1162-8

Galiforni-Silva, F., Wijnberg, K. M., de Groot, A. V., & Hulscher, S. J. M. H. (2019). The effects of beach width variability on coastal dune development at decadal scales. *Geomorphology*, *329*, 58–69. https://doi.org/10.1016/j.geomorph.2018.12.012

Gillies, J. A., Nickling, W. G., & King, J. (2002). Drag coefficient and plant form response to wind speed in three plant species: Burning Bush (*Euonymus alatus*), Colorado Blue Spruce (*Picea pungens glauca*.), and Fountain Grass (*Pennisetum setaceum*). *Journal of Geophysical Research*, *107*(D24), 4760. https://doi.org/10.1029/2001JD001259

Gillies, J. A., Nield, J. M., & Nickling, W. G. (2014). Wind speed and sediment transport recovery in the lee of a vegetated and denuded nebkha within a nebkha dune field. *Aeolian Research*, *12*, 135–141. https://doi.org/10.1016/j.aeolia.2013.12.005

Goldstein, E. B., Moore, L. J., & Durán, O. (2017). Lateral vegetation growth rates exert control on coastal foredune hummockiness and coalescing time. *Earth Surface Dynamics*, *5*, 417–427. https://doi.org/10.5194/esurf-5-417-2017

Hacker, S. D., Jay, K. R., Cohn, N., Goldstein, E. B., Hovenga, P. A., Itzkin, M., et al. (2019). Species-specific functional morphology of four US Atlantic coast dune grasses: Biogeographic implications for dune shape and coastal protection. *Diversity*, *11*(5), 1–16. https://doi.org/10.3390/d11050082

Hacker, S. D., Zarnetske, P., Seabloom, E., Ruggiero, P., Mull, J., Gerrity, S., & Jones, C. (2012). Subtle differences in two non-native congeneric beach grasses significantly affect their colonization, spread, and impact. *Oikos*, *121*(1), 138–148. https://doi.org/10.1111/j.1600-0706.2011.18887.x

Hallin, C., van IJzendoorn, C., Homberger, J.-M., & de Vries, S. (2023). Simulating surface soil moisture on sandy beaches. *Coastal Engineering*, *185*, 104376. https://doi.org/10.1016/j.coastaleng.2023.104376

Hesp, P. A. (1983). Morphodynamics of incipient foredunes in N.S.W., Australia. *Developments in Sedimentology*, *38*, 325–342. https://doi.org/10.1016/S0070-4571(08)70802-1

Hesp, P. A. (1989). A review of biological and geomorphological processes involved in the initiation and development of incipient foredunes. *Proceedings of the Royal Society of Edinburgh - Section B: Biological Sciences*, *96*, 181–201. https://doi.org/10.1017/S0269727000010927

Hesp, P. A. (2002). Foredunes and blowouts: Initiation, geomorphology and dynamics. *Geomorphology*, *48*(1–3), 245–268. https://doi.org/10.1016/S0169-555X(02)00184-8

Hesp, P. A., Dong, Y., Cheng, H., & Booth, J. L. (2019). Wind flow and sedimentation in artificial vegetation: Field and wind tunnel experiments. *Geomorphology*, *337*, 165–182. https://doi.org/10.1016/j.geomorph.2019.03.020

Hesp, P. A., & Smyth, T. A. G. (2017). Nebkha flow dynamics and shadown dune formation. *Geomorphology*, *282*, 27–38. https://doi.org/10.1016/j.geomorph.2016.12.026

Hoonhout, B. M., & de Vries, S. (2016). A process-based model for aeolian sediment transport and spatiotemporal varying sediment availability. *Journal of Geophysical Research: Earth Surface*, *121*(8), 1555–1575. https://doi.org/10.1002/2015JF003692

Hovenga, P. A., Ruggiero, P., Itzkin, M., Jay, K. R., Moore, L., & Hacker, S. D. (2022). Quantifying the relative influence of coastal foredune growth factors on the U.S. Mid-Atlantic Coast using field observations and the process-based numerical model Windsurf. *Coastal Engineering*, *181*, 104272. https://doi.org/10.1016/j.coastaleng.2022.104272

Jay, K. R., Hacker, S. D., Hovenga, P. A., Moore, L. J., & Ruggiero, P. (2022). Sand supply and dune grass species density affect Foredune shape along the US Central Atlantic Coast. *Ecosphere*, *13*(10), e4256. https://doi.org/10.1002/ecs2.4256

Judd, M. J., Raupach, M. R., & Finnigan, J. J. (1996). A wind tunnel study of turbulent flow around single and multiple windbreaks, part I: Velocity fields. *Bound. Layer Meteorol*, *80*(1–2), 127–165. https://doi.org/10.1007/BF00119015

Keijsers, J. G. S., De Groot, A. V., & Riksen, M. J. P. M. (2015). Vegetation and sedimentation on coastal foredunes. *Geomorphology*, *228*, 723–734. https://doi.org/10.1016/j.geomorph.2014.10.027

Keijsers, J. G. S., De Groot, A. V., & Riksen, M. J. P. M. (2016). Modeling the biogeomorphic evolution of coastal dunes in response to climate change. *Journal of Geophysical Research: Earth Surface*, *121*(6), 1161–1181. https://doi.org/10.1002/2015JF003815

Kroy, K., Sauermann, G., & Herrmann, H. J. (2002). Minimal model for aeolian sand dunes. *Physical Review Letters*, *88*(5), 054301. https://doi.org/10.1103/PhysRevLett.88.054301

Laporte-Fauret, Q., Askerooth, R., Wengrove, M., Hacker, S. D., Ruggiero, P., Dickey, J., et al. (2023). Experimental test of the influence of native and non-native plant species on sand accretion on a U.S. Pacific Northwest dune. In *The proceedings of the coastal sediments 2023* (pp. 627–641). https://doi.org/10.1142/9789811275135_0059

Laporte-Fauret, Q., Lubac, B., Castelle, B., Michalet, R., Marieu, V., Bombrun, L., et al. (2020). Classification of Atlantic coastal sand dune vegetation using in situ, UAV, and airborne hyperspectral data. *Remote Sensing*, *12*(14), 2222. https://doi.org/10.3390/rs12142222

Laporte-Fauret, Q., Wengrove, M., Ruggiero, R., Hacker, S. D., Cohn, N., Zarnetske, P. L., & Piercy, C. P. (2024). AeoLiS Release (Version 2.1.0) with implementations in the vegetation module and the vegetation grids [Software and Dataset]. *Zenodo*. https://zenodo.org/records/13930739

Leenders, J. K., Sterk, G., & Van Boxel, J. H. (2011). Modelling wind-blown sediment transport around single vegetation elements. *Earth Surface Processes and Landforms*, *36*(9), 1218–1229. https://doi.org/10.1002/esp.2147

Lionello, P., Sanna, A., Elvini, E., & Mufato, R. (2006). A data assimilation procedure for operational prediction of storm surge in the northern Adriatic Sea. *Continental Shelf Research*, *26*(4), 539–553. https://doi.org/10.1016/j.csr.2006.01.003

Luijendijk, A., Hagenaars, G., Ranasinghe, R., Baart, F., Donchyts, G., & Aarninkhof, S. (2018). The state of the world's beaches. *Scientific Reports*, *8*(1), 6641. https://doi.org/10.1038/s41598-018-24630-6

Luna, M. C. M., Parteli, E. J., Durán, O., & Herrmann, H. J. (2011). Model for the Genesis of coastal dune fields with vegetation. *Geomorphology*, *129*(3–4), 215–224. https://doi.org/10.1016/j.geomorph.2011.01.024

Martinez, M. L., Hesp, P., & Gallego-Fernandez, J. B. (2013). Coastal dunes: Human impact and need for restoration. In M. L. Martinez, J. B. Gallego-Fernández, & P. Hesp (Eds.), *Restoration of coastal dunes* (pp. 1–14). Springer. https://doi.org/10.1007/978-3-642-33445-0_1

Marzialetti, F., Giulio, S., Malavasi, M., Sperandii, M. G., Rosario Acosta, A. T., & Carranza, M. L. (2019). Capturing coastal dune natural vegetation types using a phenology-based mapping approach: The potential of Sentinel-2. *Remote Sensing*, *11*(12), 1506. https://doi.org/10.3390/rs11121506

Maun, M. A. (1998). Adaptations of plants to burial in coastal sand dunes. *Canadian Journal of Botany*, *76*(5), 713–738. https://doi.org/10.1139/b98-058

Maun, M. A., & Perumal, J. (1999). Zonation of vegetation on lacustrine coastal dunes: Effects of burial by sand. *Ecology Letters*, *2*(1), 14–18. https://doi.org/10.1046/j.1461-0248.1999.21048.x

Mayaud, J. R., & Webb, N. P. (2017). Vegetation in drylands: Effects on wind flow and Aeolian sediment transport. *Land*, *6*(3), 64. https://doi.org/10.3390/land6030064

Mayaud, J. R., Wiggs, G. F. S., & Bailey, R. M. (2016). Characterizing turbulent wind flow around dryland vegetation. *Earth Surface Processes and Landforms*, *41*(10), 1421–1436. https://doi.org/10.1002/esp.3934

Merkens, J. L., Lincke, D., Hinkel, J., Brown, S., & Vafeidis, A. T. (2018). Regionalization of population growth projections in coastal exposure analysis. *Climate Change*, *151*(3–4), 413–426. https://doi.org/10.1007/s10584-018-2334-8

Middleton, G. V., & Southard, J. B. (1984). *Mechanics of sediment movement* (2nd ed., p. 401). Society of Economic Paleontologists and Mineralogists.

Miri, A., Dragovich, D., & Dong, Z. (2017). Vegetation morphologic and aerodynamic characteristics reduce aeolian erosion. *Scientific Reports*, *7*(1), 12831. https://doi.org/10.1038/s41598-017-13084-x

Miri, A., Dragovich, D., & Dong, Z. (2018). The response of live plants to airflow–Implication for reducing erosion. *Aeolian Res*, *33*, 93–105. https://doi.org/10.1016/j.aeolia.2018.06.002

Miri, A., Dragovich, D., & Dong, Z. (2019). Wind-borne sand mass flux in vegetated surfaces–wind tunnel experiments with live plants. *Catena*, *172*, 421–434. https://doi.org/10.1016/j.catena.2018.09.006

Moore, L. J., Durán, O., & Ruggiero, P. (2016). Vegetation control allows autocyclic formation of multiple dunes on prograding coasts. *Geology*, *44*(7), 559–562. https://doi.org/10.1130/G37778.1

Neumann, B., Vafeidis, A. T., Zimmermann, J., & Nicholls, R. J. (2015). Future coastal population growth and exposure to sea-level rise and coastal flooding - A global assessment. *PLoS One*, *10*(3), e0131375. https://doi.org/10.1371/journal.pone.0118571

Nordstrom, K. F. (2000). *Beaches and dunes of developed coasts* (p. 347). Cambridge University Press. https://doi.org/10.1017/CBO9780511549519

Okin, G. S. (2008). A new model of wind erosion in the presence of vegetation. *Journal of Geophysical Research*, *113*(F2), F02S10. https://doi.org/10.1029/2007JF000758

Parteli, E. J. R., Durán, O., Tsoar, H., Schwämmle, V., & Herrmann, H. J. (2009). Dune formation under bimodal winds. *Proceedings of the National Academy of Sciences*, *106*(52), 22085–22089. https://doi.org/10.1073/pnas.0808646106

Provoost, S., Jones, M. L. M., & Edmondson, S. E. (2011). Changes in landscape and vegetation of coastal dunes in northwest Europe: A review. *Journal of Coastal Conservation*, *15*(1), 207–226. https://doi.org/10.1007/s11852-009-0068-5

Pye, K., Blott, S. J., & Howe, M. A. (2014). Coastal dune stabilization in Wales and requirements for rejuvenation. *Journal of Coastal Conservation*, *18*(1), 27–54. https://doi.org/10.1007/s11852-013-0294-8

Raupach, M. R. (1992). Drag and drag partition on rough surfaces. *Boundary-Layer Meteorology*, *60*(4), 375–395. https://doi.org/10.1007/BF00155203

Raupach, M. R., Gillette, D. A., & Leys, J. F. (1993). The effect of roughness elements on wind erosion threshold. *Journal of Geophysical Research*, *98*(D2), 3023–3029. https://doi.org/10.1029/92JD01922

Reijers, V. C., Siteur, K., Hoeks, S., van Belzen, J., Borst, A. C. W., Heusinkveld, J. H. T., et al. (2019). A Lévy expansion strategy optimizes early dune building by beach grasses. *Nature Communications*, *10*(1), 2656. https://doi.org/10.1038/s41467-019-10699-8

Roelvink, D., & Costas, S. (2019). Coupling nearshore and aeolian processes: XBeach and duna process-based models. *Environmental Modelling & Software*, *115*, 98–112. https://doi.org/10.1016/j.envsoft.2019.02.010

Rojas, R., Feyen, L., Bianchi, A., & Dosio, A. (2012). Assessment of future flood hazard in Europe using a large ensemble of bias corrected regional climate simulations. *Journal of Geophysical Research*, *117*(D17), 1–22. https://doi.org/10.1029/2012JD017461

Rominger, J. T., & Nepf, H. M. (2011). Flow adjustment and interior flow associated with a rectangular porous obstruction. *Journal of Fluid Mechanics*, *680*, 636–659. https://doi.org/10.1017/jfm.2011.199

Sauermann, G., Kroy, K., & Herrmann, H. J. (2001). Continuum saltation model for sand dunes. *Physics Reviews E.*, *64*(3), 031305. https://doi.org/10.1103/PhysRevE.64.031305

Schwämmle, V., & Herrmann, H. J. (2005). A model of Barchan dunes including lateral shear stress. *European Physical Journal E: Soft Matter*, *16*(1), 57–65. https://doi.org/10.1140/epje/e2005-00007-0

Seabloom, E. W., Ruggiero, P., Hacker, S. D., Mull, J., & Zarnetske, P. L. (2013). Invasive grasses, climate change, and exposure to storm-wave overtopping in coastal dune ecosystems. *Global Change Biology*, *19*(3), 824–832. https://doi.org/10.1111/gcb.12078

Shao, Y. (2008). *Physics and modelling of wind erosion* (Vol. 37). Springer. https://doi.org/10.1007/978-1-4020-8895-7

Sherman, D. J., & Bauer, O. (1993). Dynamics of beach-dune systems. *Progress in Physical Geography*, *17*(4), 413–447. https://doi.org/10.1177/030913339301700402

Stepanek, J. (2023). Carbon storage in U.S. Pacific Northwest Coastal dunes: The role of invasive beachgrasses and sand supply MS Thesis. Oregon State University.

Stive, M. J. F., Aarninkhof, S. G. J., Hamm, L., Hanson, H., Larson, M., Wijnberg, K. M., et al. (2002). Variability of shore and shoreline evolution. *Coastal Engineering*, *47*(2), 211–235. https://doi.org/10.1016/S0378-3839(02)00126-6

Strypsteen, G., van Rijn, L. C., Hoogland, M. D., Rauwoens, P., Fordeyn, J., Hijma, M. P., & Lodder, Q. J. (2021). Reducing aeolian sand transport and beach erosion by using armour layer of coarse materials. *Coastal Engineering*, *166*, 103871. https://doi.org/10.1016/j.coastaleng.2021.103871

Suir, G. M., Jackson, S., Saltus, C., & Reif, M. (2023). Multi-temporal trend analysis of coastal vegetation using metrics derived from hyperspectral and LiDAR data. *Remote Sensing*, *15*(8), 2098. https://doi.org/10.3390/rs15082098

Van Oene, H., Berendse, F., & de Kovel, C. G. F. (1999). Model analysis of the effects of historic CO_2 levels and nitrogen inputs on vegetation succession. *Ecological Applications*, *9*(3), 920–935. https://doi.org/10.1890/1051-0761(1999)009[0920:MAOTEO]2.0.CO;2

Van Rijn, L. C., & Strypsteen, G. (2020). A fully predictive model for aeolian sand transport. *Coastal Engineering*, *156*, 103600. https://doi.org/10.1016/j.coastaleng.2019.103600

Vollsinger, S., Mitchell, S. J., Byrne, K. E., Novak, M. D., & Rudnicki, M. (2005). Wind tunnel measurements of crown streamlining and drag relationships for several hardwood species. *Canadian Journal of Forest Research*, *35*(5), 1238–1249. https://doi.org/10.1139/x05-051

Vousdoukas, M. I., Ranasinghe, R., Mentaschi, L., Plomaritis, T. A., Athanasiou, P., Luijendijk, A., & Feyen, L. (2020). Sandy coastlines under threat of erosion. *Nature Climate Change*, *10*(3), 260–263. https://doi.org/10.1038/s41558-020-0697-0

Vousdoukas, M. I., Voukouvalas, E., Annunziato, A., Giardino, A., & Feyen, L. (2016). Projections of extreme storm surge levels along Europe. *Climate Dynamics*, *47*(9–10), 3171–3190. https://doi.org/10.1007/s00382-016-3019-5

Walker, I. J., Davidson-Arnott, R. G. D., O'Bauer, B., Hesp, P. A., Delgado-Fernandez, I., Ollerhead, J., & Smyth, T. A. G. (2017). Scale-dependent perspectives on the geomorphology and evolution of beach-dune systems. *Earth-Science Reviews*, *171*, 220–253. https://doi.org/10.1016/j.earscirev.2017.04.011

Webb, N. P., Okin, G. S., & Brown, S. (2014). The effect of roughness elements on wind erosion: The importance of surface shear stress distribution. *Journal of Geophysical Research*, *119*(10), 6066–6084. https://doi.org/10.1002/2014JD021491

Weng, W. S., Hunt, J. C. R., Carruthers, D. J., Warren, A., Wiggs, G. F. S., Livingstone, I., & Castro, I. (1991). Air flow and sand transport over sand-dunes. In O. E. Barndorff-Nielsen & B. B. Willetts (Eds.), *Aeolian grain transport*, *Acta Mechanica Supplementum* (Vol. 2, pp. 1–22). Springer. https://doi.org/10.1007/978-3-7091-6703-8_1

Wiedemann, A. M., & Pickart, A. (1996). The Ammophila problem on the Northwest coast of North America. *Landscape and Urban Planning*, *34*(3–4), 287–299. https://doi.org/10.3390/d13120629

Willmott, C. J. (1981). On the validation of models. *Physical Geography*, *2*, 184–194. https://doi.org/10.1080/02723646.1981.10642213

Wolfe, S. A., & Nickling, W. G. (1993). The protective role of sparse vegetation in wind erosion. *Progress in Physical Geography*, *17*(1), 50–68. https://doi.org/10.1177/030913339301700104

Youssef, F., Visser, S. M., Karssenberg, D., Erpul, G., Cornelis, W. M., Gabriels, D., & Poortinga, A. (2012). The effect of vegetation patterns on wind-blown mass transport at the regional scale: A wind tunnel experiment. *Geomorphology*, *159*, 178–188. https://doi.org/10.1016/j.geomorph.2012.03.023

Zarnetske, P. L., Gouhier, T. C., Hacker, S. D., Seabloom, E. W., & Bokil, V. A. (2013). Indirect effects and facilitation among native and non-native species promote invasion success along an environmental stress gradient. *Journal of Ecology*, *101*(4), 905–915. https://doi.org/10.1111/1365-2745.12093

Zarnetske, P. L., Hacker, S. D., Seabloom, E. W., Ruggiero, P., Killian, J. R., Maddux, T. B., & Cox, D. (2012). Biophysical feedback mediates effects of invasive grasses on coastal dune shape. *Ecology*, *93*(6), 1439–1450. https://doi.org/10.1890/11-1112.1

Zarnetske, P. L., Ruggiero, P., Seabloom, E. W., & Hacker, S. D. (2015). Coastal foredune evolution: The relative influence of vegetation and sand supply in the US Pacific Northwest. *Journal of the Royal Society Interface*, *12*(106), 20150017. https://doi.org/10.1098/rsif.2015.0017

Zhang, N., Kang, J. H., & Lee, S. J. (2010). Wind tunnel observation on the effect of a porous wind fence on shelter of saltating sand particles. *Geomorphology*, *120*(3–4), 224–232. https://doi.org/10.1016/j.geomorph.2010.03.032